Triple Scissor Extender: A 6-DOF Lifting and Positioning Robot for Autonomous Aircraft Manufacturing

by

Daniel Jesus Gonzalez

S.B., Massachusetts Institute of Technology (2014)

MASSACHUSETTS INSTITUTE
OF TECHNOLOGY
JUN 02 2016
LIBRARIES
ARCHIVES

Submitted to the Department of Mechanical Engineering
in partial fulfillment of the requirements for the degree of

Master of Science in Mechanical Engineering

at the

MASSACHUSETTS INSTITUTE OF TECHNOLOGY

June 2016

© Massachusetts Institute of Technology 2016. All rights reserved.

Author .... Signature redacted
Department of Mechanical Engineering
May 6, 2016

Certified by............ Signature redacted ...
H. Harry Asada
Ford Professor of Engineering
Thesis Supervisor

Accepted by .... Signature redacted
Rohan Abeyaratne
Quentin Berg Professor of Mechanics
Graduate Officer

MIT Libraries

77 Massachusetts Avenue
Cambridge, MA 02139
http://libraries.mit.edu/ask

DISCLAIMER NOTICE

Due to the condition of the original material, there are unavoidable flaws in this reproduction. We have made every effort possible to provide you with the best copy available.

Thank you.

The images contained in this document are of the best quality available.

Triple Scissor Extender: A 6-DOF Lifting and Positioning Robot for Autonomous Aircraft Manufacturing

by

Daniel Jesus Gonzalez

Submitted to the Department of Mechanical Engineering
on May 6, 2016, in partial fulfillment of the
requirements for the degree of
Master of Science in Mechanical Engineering

Abstract

This thesis presents the Triple Scissor Extender (TSE), a novel 6-DOF robotic mechanism for reaching high ceilings and positioning an end-effector. The end-effector is supported with three scissor mechanisms that extend towards the ceiling with 6 independent linear actuators moving the base ends of the individual scissors. The top point of each scissor is connected to one of three ball joints located at the three vertices of the top triangular plate holding the end-effector. Coordinated motion of the 6 linear actuators at the base allows the end-effector to reach an arbitrary position with an arbitrary orientation. The design concept of the Triple Scissor Extender is presented, followed by kinematic modeling and analysis of the the Inverse Jacobian relating actuator velocities to the end-effector velocities. The Inverse Jacobian eigenvalues are determined for diverse configurations in order to characterize the kinematic properties. The sensitivity of the Inverse Jacobian Eigenvalues to the various non-dimensionalized design parameters is discussed. A proof-of-concept prototype has been designed and built. The detailed mechanical and electrical design, manufacture, and assembly is described, and the control software is discussed. The Inverse Jacobian for use in differential control is evaluated through experiments. A method for extending the functionality of the TSE by using multiple interchangeable end effectors is presented. The detailed design, manufacture, assembly, and testing of one such end effector, the Fastener Robot (FASBot), is described, and its performance characterized.

Thesis Supervisor: H. Harry Asada
Title: Ford Professor of Engineering

Acknowledgments

I would like to thank my mother and father, who have dedicated themselves to shaping me to become the person I am proud to be today. I hope I've made you proud, not only of any academic or professional success I may have achieved, but of my character, which I hope reflects my upbringing in your warm arms. I'm very lucky to have you!

I would like to thank Maura Hennessey for her limitless support throughout the entirety of my Master's degree journey. I've grown as a person through your influence, and I cherish every moment shared with you, especially if it was over a cup of tea!

I would like to thank my friends and housemates for their encouragement and companionship, for always showing me kindness and understanding, and for growing with me both as engineers and as people.

I would like to thank my wonderful labmates of the d'Arbeloff Lab, for being a pleasure to work with, for providing insightful feedback on my research, and for making my workplace more fun than it has any right to be!

I would like to thank Patrick McAtamney and Thomas Villalon, shop instructors of the Edgerton Center Area 51 CNC shop, for assisting me with fabrication.

I would like to thank Rebecca Li, Madame President of the MIT Combat Robotics Club and the MIT Electronics Research Society, for both her friendship and late-night machine shop access.

I would like to thank the people of the MIT Electronics Research Society for teaching me, encouraging me, and providing a playground to learn all of the engineering that I can't learn in the classroom. You have being such a welcoming group, and I will always remember the many late nights working, talking, relaxing, and learning with you.

I would like to thank Professor Alexander H. Slocum for showing me the beauty of deterministic machine design, and for teaching me lessons on life in the process. Our lives are short, and thus our engineering should be deterministic, elegant, and concise, so that we may have more time to enjoy snowboarding!

I would like to thank Charles Guan, for being my first real inspiration to become

a mechanical designer. I will probably carry the lessons I've learned from you for as long as I am an engineer. You've also been a generous friend, and I wish you the very best in your post-MIT career.

I would like to thank the late Professor Seth Teller for being the first person to show me what the current state of the wonderful field of robotics was all about. You always encouraged me to take advantage of the insight my mechanical engineering background gave me in the design and implementation of robotic systems, and you inspired me to pursue a career in advancing the field of robotics. Thank you for everything. Rest in peace.

Finally, I would like to thank Professor H. Harry Asada, whose ambition and endless steam of ideas, while challenging to keep up with, always complement and inspire my own. You are shaping me to become a better mathematician, engineer, roboticist, and researcher.

Contents

1 **Introduction** **13**

1.1 Background and Motivation: Autonomous Aircraft Manufacturing . . 16

1.2 Contributions and Overview 18

2 **Triple Scissor Extender Design Concept and Geometry Overview** **21**

2.1 Concept and Geometry 21

2.2 Modes of Motion 24

3 **Modeling** **27**

3.1 Kinematics 27

3.1.1 The Inverse Kinematics Problem 27

3.1.2 General Kinematic Constraint Derivation 31

3.1.3 Nondimensionalized Kinematic Equations 35

3.2 Formulation of the Inverse Jacobian 36

3.2.1 Characterizing the TSE Kinematic Properties 36

3.2.2 Computation of the Jacobians 38

4 **Analysis** **41**

4.1 Differential Motion and Manipulability Analysis through Spatial Gear Ratios 41

4.2 Design Parameter Sensitivity Analysis 44

4.2.1 Sensitivity due to scissor length ratio k_1 45

4.2.2 Sensitivity due to Actuator Angle k_2 46

4.2.3 Sensitivity due to Actuator Coordinate Radius k_3 48

5 Detailed Design of Prototype 51

5.1 Static Loading Analysis and Actuator Specifications 52

5.2 Structure, Joint, and Linkage Design 54

5.3 Manufacturing and Assembly 58

5.4 Electronics, Controls, and Software 60

6 Experimental Validation of Differential Motion 63

6.1 Procedure 63

6.2 Results 64

7 Extending Functionality with Detachable End Effectors: FASBots 67

7.1 FASBot Requirements 67

7.2 FASBot Detailed Design 69

7.2.1 Clamping and Axis Design Details 69

7.2.2 Coupling to the Fuselage and to the Triple Scissor Extender . 72

7.3 FASBot Manufacturing and Assembly 73

7.4 FASBot Testing and Results 76

8 Conclusion and Future Work 83

8.1 Conclusion 83

8.2 Recommendations for Future Work 84

List of Figures

1-1 The Boeing FAUB system, which uses robots made by KUKA. 13

1-2 Triple Scissor Extender 14

1-3 A Traditional Scissor Lift for Raising Passengers 15

1-4 Demonstration of the Triple Scissor Extender's large height range . . 15

1-5 The outside of a barrel section of the Boeing 787 Dreamliner on display in Seattle, WA, USA. 16

1-6 The longitudinal stringers and circumferential shear ties of a Boeing 787. 17

2-1 Kinematic parameters of a single scissor mechanism. 22

2-2 Top view of the scissor coordinate system and explanation of the design parameters η and $r_{actuator}$ 23

2-3 Some example linear actuator configurations for various η 23

2-4 Top plate radius $r_{actuator}$ and linear slide dimensions of the TSE. . . . 24

2-5 Intuitive Coordinated Motion Patterns of the Triple Scissor Extender 25

3-1 Base and end effectors coordinate systems 28

3-2 Projection of Relevant Points onto the Base Plane 29

3-3 Inverse Kinematics being solved numerically in simulation 30

3-4 Top View of Base Plane showing Projected Point H on O_1xy-plane . 32

4-1 Jacobian at Various Heights along z-axis 42

4-2 Jacobian Ellipsoids for points along z-axis. 43

4-3 Jacobian Ellipsoids for points at constant $z = 914.40$ millimeters . . . 44

4-4 Jacobian Eigenvalues with Changing Length Ratio 45

4-5 Jacobian Eigenvalues with Changing Length Ratio (Zoomed In Near k_1 of Prototype) 46
4-6 Jacobian Eigenvalues with Changing Length Ratio (Zoomed In Near $k_1 = 1$) 47
4-7 Jacobian Eigenvalues with changing Slide Angle 48
4-8 Jacobian Eigenvalues with changing Slide Angle (Log Scale) 49
4-9 Jacobian Eigenvalues with changing Slide Angle for larger k_1 49
4-10 Jacobian Eigenvalues with changing Actuator Coordinate System Radius 50

5-1 Simplified models and Free Body Diagram of the Triple Scissor Extender worst-case loading situations. 52
5-2 Individual actuator force F_{act} required to bear a total load of 50 pounds at a given angle θ 53
5-3 Section view of the Parker OSPE 32 SB Actuator 54
5-4 A single scissor mechanism, and the forces it must bear. 55
5-5 Section view of a single joint of the TSE scissor linkages. 55
5-6 Regular and Section view of the Ball joint interfacing the top of each scissor mechanism with each apex of the top platform. 56
5-7 Plastic Bottom Ball Joint Adapters for coupling each scissor mechanism bottom ball joint to its respective linear actuator. 56
5-8 Finite Element Analysis of the Bottom Ball Joint Adapters. 57
5-9 Solid Model Rendering of the Triple Scissor Extender 58
5-10 The Top and Bottom Plates being cut on an Omax 5555 waterjet. . . 59
5-11 Set of scissor mechanism parts cut on the waterjet and partially assembled 60
5-12 Experimental Prototype 61
5-13 Copley Controls Accelnet panel chosen to control and drive the Parker actuators. 61

6-1 Experimental Setup 64
6-2 Top Platform Desired and Measured Translation vs Time 65

7-1 The final FASBot CAD rendering. 68
7-2 Section view of the Z-Axis. Both axes and clamps have the same linear carriage design. 70
7-3 Section View of the driven Clamp Axis. 71
7-4 Side View Rendering of the FASBot. 71
7-5 The five point contacts used for coupling to the fuselage. 72
7-6 CAD Rendering of the FASBot clamped to the fuselage facade. 73
7-7 The components were cut from an Epilog lasercutter. 74
7-8 Closeup of the X and Z axes after assembly. 75
7-9 The twin clamp axes assembled with the timing belt that couples their motion. 76
7-10 The electronics compartment of the FASBot. 77
7-11 The fully assembled FASBot. 78
7-12 The FASBot during the various stages of use. 79
7-13 The Three-grooves/three-ball FASBot-to-Triple Scissor Extender Kinematic Coupling. 79
7-14 The experimental setup for testing axis repeatability. 80
7-15 Three runs of the repeatability test, combined and individual plots. . 81

8-1 Example of Error Modeling for Stiffness Analysis of a single Beam . . 84
8-2 Example of Error Modeling for Stiffness Analysis for a cascaded series of beams 86

Chapter 1

Introduction

Industrial automation applications requiring both a high payload capacity and a large workspace typically rely on large serial link articulated robots. While these robots are an excellent choice for factory floors with ample maneuvering space, they are often too heavy for mobile applications and unable to reach the desired workspace in confined settings.

For example, a stationary articulated robot arm can easily perform various operations along the outside of a commercial aircraft fuselage as it is being assembled, but this same arm cannot be easily placed on a mobile base and rolled *into* the fuselage barrel to perform additional operations: the arm is simply too large and heavy to make this a robust solution. Current systems have limited payload and workspace due to these limitations (See Figure 1-1)

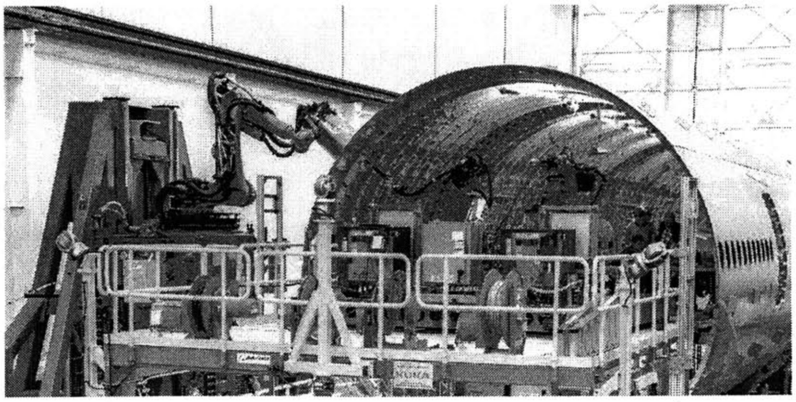

Figure 1-1: The Boeing FAUB system, which uses robots made by KUKA.

Parallel manipulators such as the 6-DOF Gough-Stewart hexapod platform [2] [10], are small and light relative to their load-bearing capacity, unlike articulated serial-link arms. These advantages make the 6-DOF parallel manipulator a candidate for confined-space maneuvering and assembly, but they have small workspaces due to the use of piston-style prismatic actuators as their linkages. A fully-retracted Parallel Platform of unit height h cannot reach past $2h$ because its actuators cannot extend any more than twice their smallest length.

To address this limitation, scissor mechanisms can be used to amplify the height range. A 3-DOF example of this concept is analyzed in [12]. We designed a new class of 6-DOF parallel platform that uses parallel scissor mechanisms to achieve a large workspace compared to its original size while maintaining the benefits of most parallel manipulators. Three scissor lift mechanisms are combined so that the end-effector can be supported by them in parallel and the position and orientation of the end-effector can be controlled arbitrarily in 3-dimensional space.

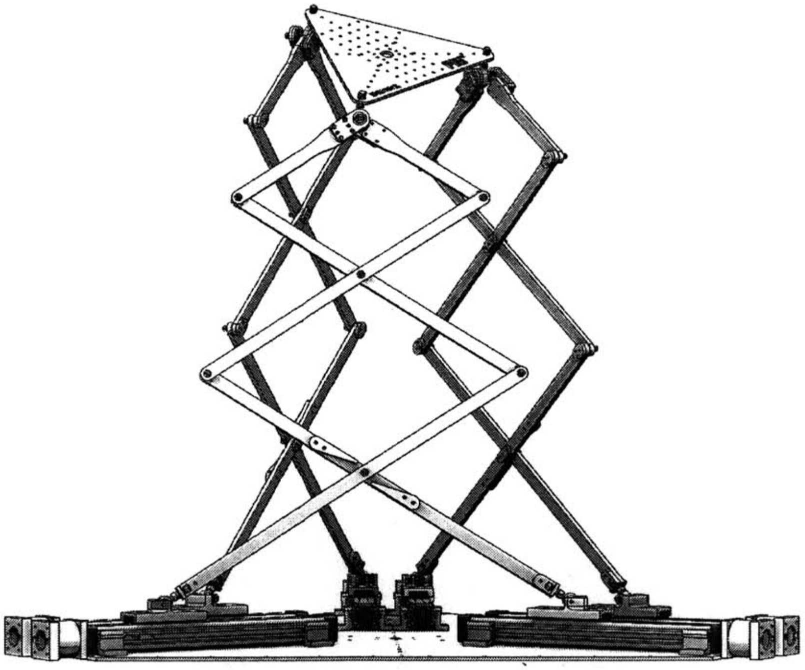

Figure 1-2: Triple Scissor Extender

This Triple Scissor Extender (TSE) (see Figure 1-2) is particularly useful both for reaching high ceilings or walls and positioning/orienting its end-effector freely within

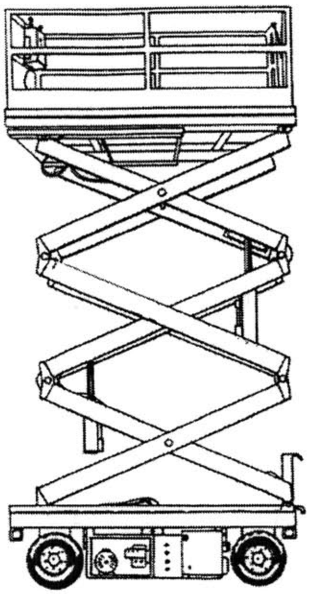

Figure 1-3: A Traditional Scissor Lift for Raising Passengers

a working space. When the TSE is fully contracted, the whole structure becomes compact, making it easy for transportation. At full extension, the device height becomes many times greater than its original height (like a traditional 1-DOF aerial scissor lift commonly used for maintenance, assembly, and construction, see Figure 1-3), allowing it to reach high ceilings and walls (See Figure1-4).

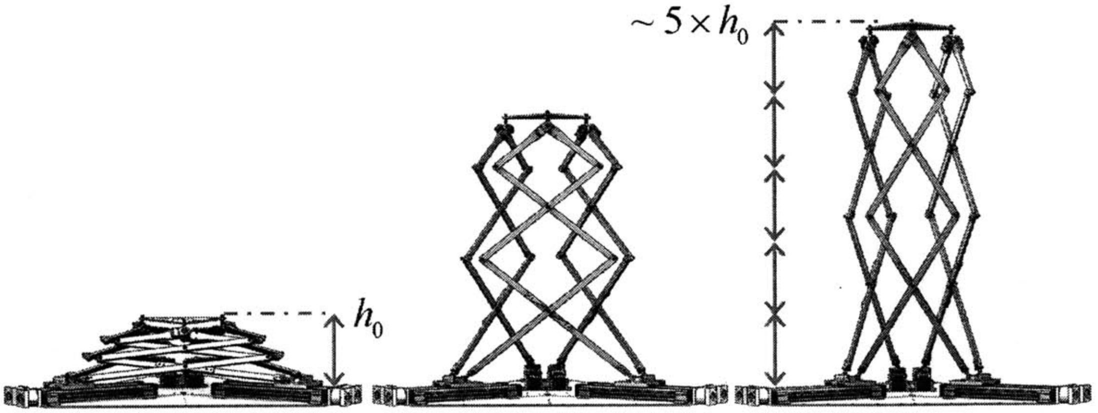

Figure 1-4: Demonstration of the Triple Scissor Extender's large height range

1.1 Background and Motivation: Autonomous Aircraft Manufacturing

Despite the high availability of industrial manufacturing machines and robots, aircraft are still mostly assembled by hand. The machining and assembly tolerances of aircraft can vary significantly from one plane to another other due to unmodeled deformations, as well as from one location to another along the same airframe. Automation equipment must constantly be touching off and recalibrating in order to prevent tool crashes and stay true to the intended design. These constant stalls are a bottleneck for the aircraft manufacturing and assembly process, and limit the productivity of any factory producing large aircraft.

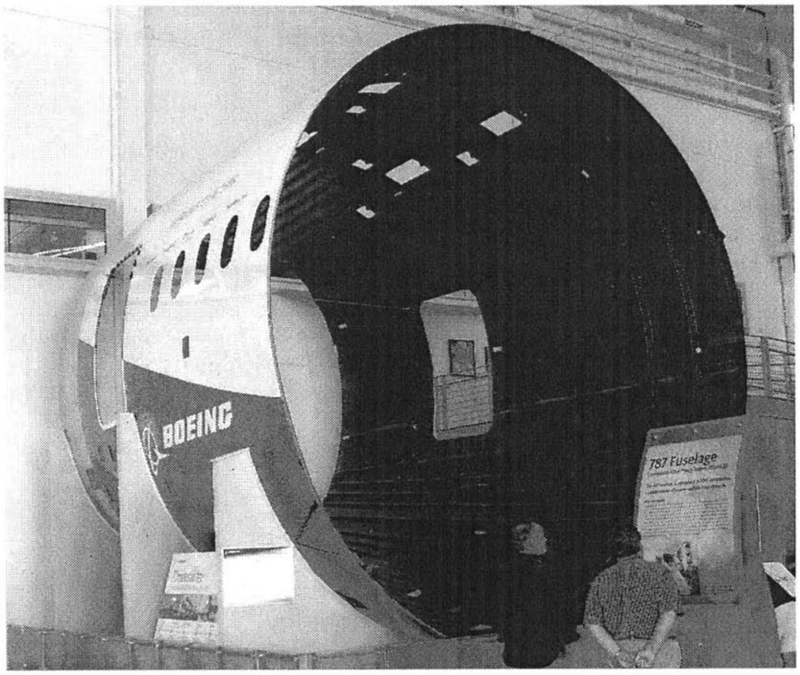

Figure 1-5: The outside of a barrel section of the Boeing 787 Dreamliner on display in Seattle, WA, USA.

One of the most time-costly operations for manufacturing commercial aircraft is the installation of fasteners that couple the main load-bearing members of the fuselage. The Boeing 787 aircraft's main fuselage barrel skin is a single piece of composite (see Figure 1-5). Longitudinal trapezoid-profile stringers, also made from composite fibers, provide bending strength and are cured with the skin. For additional strength under pressure, the fuselage has composite ribs called shear ties.

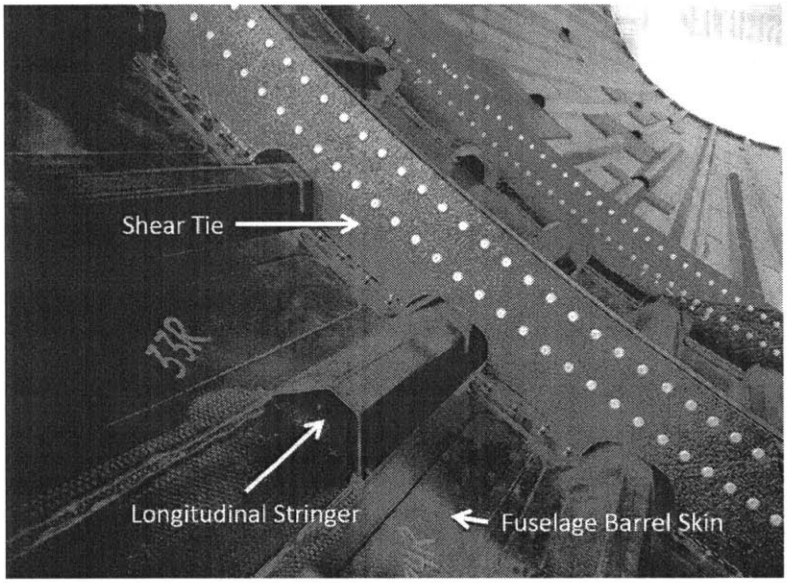

Figure 1-6: The longitudinal stringers and circumferential shear ties of a Boeing 787.

These shear ties are placed and temporarily installed with tack fasteners by hand. Then thousands of holes (see Figure 1-6) are drilled through both the skin and shear tie. They are reamed and countersunk before flush Hi-Lok fasteners are inserted from the outside. From the inside, the Hi-Lok frangible collars are installed using standard tools.

The current fastener installation process takes 6 days to complete using automation equipment that can only install one fastener at a time and requires constant recalibration. This method of fastener installation is currently a bottleneck in the total assembly process. By allowing the automation equipment to continuously relocalize and intelligently work with the outside robots, and by parallelizing the fastener installation process by introducing more autonomous agents, this bottleneck can be overcome and the factory can achieve higher throughput.

1.2 Contributions and Overview

This thesis presents the Triple Scissor Extender (TSE), a novel 6-DOF mechanism that uses scissor linkages to amplify its height range. Chapter 2 explains in detail the concept of extending the workspace of a 6-DOF parallel manipulator with pantograph/scissor mechanisms and the inventive design of the TSE.

Chapter 3 provides kinematic modeling and design parametrization of the TSE. The geometry that defines the design parameters are explained, and the relationship between the 6 actuator inputs and the 6-DOF 3D pose, that is, the combined position and orientation, of the top platform are revealed through the Kinematic Constraint Equations, which are derived for both the general case and for the implemented Delta design. These equations may be written in a non-dimensionalized form to easily analyze the differences between implementations with differing design parameters. The Inverse Kinematics can be solved using these constraint equations. The Inverse Jacobian Matrix, which characterizes the linear differential relationship between the inputs and outputs of the TSE system about a home position, is derived from the Kinematic Constraint Equations.

In Chapter 4, the behavior of the TSE is analyzed using the mathematical models developed in Chapter 3. Singular Value Decomposition is performed on the Inverse Jacobian Matrix in order to reveal important properties of the TSE about these home positions for the implemented design. The sensitivity of the Inverse Jacobian Eigenvalues to the various non-dimensionalized design parameters is discussed.

The detailed design and implementation of the prototype is discussed in Chapter 5. The functional requirements of the machine are stated, and analyses are performed in order to specify and design the structure, joints, linkages, and actuation to meet these functional requirements. The manufacture and assembly of the TSE is detailed, and the implementation of the control software and electronics are discussed.

Chapter 6 discusses the experimental validation of positioning accuracy using the Inverse Jacobian control scheme, and discuss the results.

A method for extending the functionality of the TSE by using multiple interchangeable end effectors is presented in Chapter 7. The detailed design of a Fastener Robot (or FASBot), which can be carried by the TSE and clamp onto the inside of an airframe, is discussed. Details include the clamp and axis design, the airframe coupling strategy, and the manufacture and assembly. The FASBot axis motion repeatability is experimentally validated.

Chapter 8 provides a conclusion of the work done for this thesis, and recommendations for future work related to the Triple Scissor Extender.

Chapter 2

Triple Scissor Extender Design Concept and Geometry Overview

The novelty of the Triple Scissor Extender lies in the combination of two concepts: the use of the pantograph or scissor mechanism to amplify motion and the kinematics of 6-DOF parallel manipulators like the Stewart-Gough platform.

2.1 Concept and Geometry

Consider two links of length ℓ_0 existing on a plane xy joined together at one end with a rotational joint at point C. The other end of each link is attached to a rotational joint that is coupled to a linear slide located on the x-axis. Both of these linear slides s_A and s_B travel along the same line. The point we wish to control is point C, which has 2 degrees of freedom, (x_C, y_C). As inputs, we can change the position, x_A or x_B of each linear slide.

Two modes of motion exist: if both slide s_A and slide s_B move at the same velocity along the x-axis, then point C will also move at that same velocity in the x direction; if slide s_A and slide s_B move towards or away from each other with equal and opposite velocities, then point C will move only in the y direction. Through the superposition of these modes of motion, we can reach any point above the x-axis up to some maximum height.

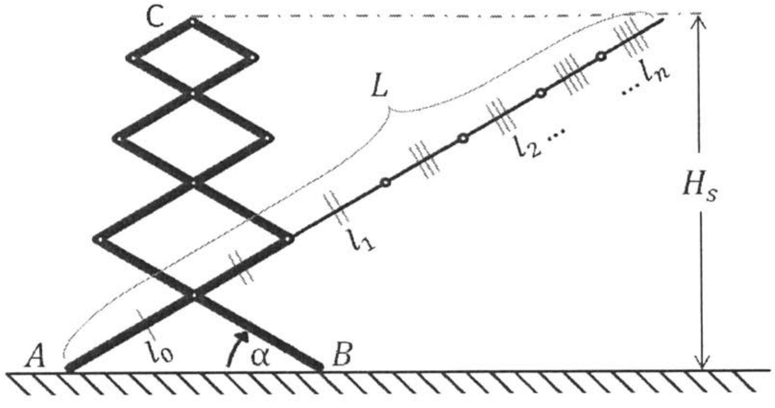

Figure 2-1: Kinematic parameters of a single scissor mechanism.

Now consider extending each link beyond point C by some smaller length ℓ_1, each with a rotational joint at the end, and then adding to those joints two more links of length ℓ_1 that are joined together at the other end, which becomes the new point C. We now have a triangle with a parallelogram on top: a basic scissor mechanism. The same two modes of motion exist as in the previous case but the ratio of inward motion of slides s_A and s_B and the vertical motion of point C has been amplified by the pantograph mechanism! Additional parallelograms of side length $\ell_2 < \ell_3 < \ldots < \ell_n$ can be added to the assembly to produce a mechanism like that in Figure 2-1.

Now we introduce the third dimension to the model and change the coordinate frame orientation such that the previous xy-plane becomes the new yz-plane, with the z-axis pointed upwards, the points A and B lying along the y-axis, and the x-axis orthogonal to the yz-plane. We turn the rotational joints at slide s_A and slide s_B into ball joints that allow the entire scissor mechanism to rotate about the line $\overline{AB}$. Ball joints are used because the scissor mechanism is required to pitch and yaw with respect to the linear slides in 3D space while moving, and must roll with respect to the linear slides in order to rotate about line $\overline{AB}$.

This motion and behavior can be achieved even if the two slides are not collinear. By changing the angle of the linear slides from the horizontal η, motion can be achieved in both the horizontal and vertical directions, in addition to changing the height of the scissor mechanism by changing the length of $\overline{AB}$. (See Figure 2-2). The linear slides that determine their motion, can be arranged at any distance $r_{actuator}$

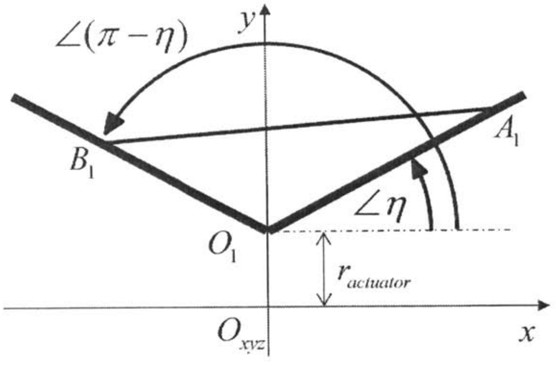

Figure 2-2: Top view of the scissor coordinate system and explanation of the design parameters η and $r_{actuator}$

apart from the center.

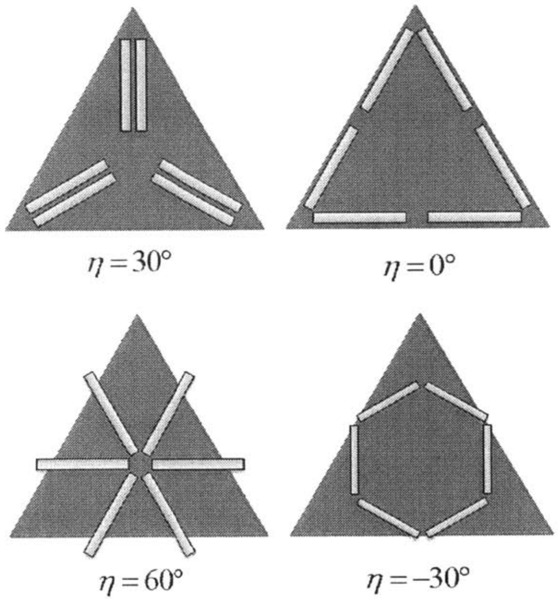
$\eta = 30°$

$\eta = 0°$

$\eta = 60°$

$\eta = -30°$

Figure 2-3: Some example linear actuator configurations for various η

Now consider the scissor mechanism's location on the new xy-plane. We introduce two identical scissor mechanisms, which we label 2 and 3, and then arrange the trio in a triangular, or Delta, configuration, where $\eta = 30°$. The linear slides can also be configured with other values of η, with some examples shown in Figure 2-3.

We introduce a small triangular top plate, and connect points C_1, C_2, and C_3 to

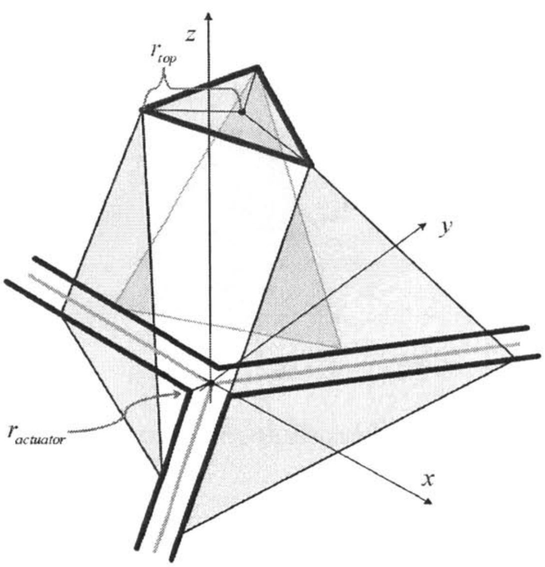

Figure 2-4: Top plate radius $r_{actuator}$ and linear slide dimensions of the TSE.

the three apices of the top plate via ball joints. As shown in Figure 2-4, the distance between the top plate center and each point C_i is r_{top}. Finally we can put the six independent linear slides s_{A1}, s_{B1}, s_{A2}, s_{B2}, s_{A3}, and s_{B3} (two per scissor) on a plane and arrange them in pairs to get the final formulation of the TSE, shown in Figure 1-2.

2.2 Modes of Motion

The top platform of the TSE has 6 DOFs. Some of these can be deduced intuitively by reasoning about the differential motion of the six slides and how they affect the pose of the top platform (see Figure 2-5). By moving only slides s_{A1} and s_{B1} inwards, point C_1 moves upwards, rotating the top platform about line $\overline{C_2C_3}$.

Similar rotations can be achieved with scissor mechanisms 2 and 3. Through a combination of these motions, the pitch and the roll of the top platform can be commanded. By moving all 6 slides inward simultaneously, the top platform translates upward. By alternating the direction of each slide sequentially, the top plate rotates about the z-axis in a yaw motion. By moving one adjacent pair of scissors outward and the remaining scissors inward, translational motion is achieved in the average

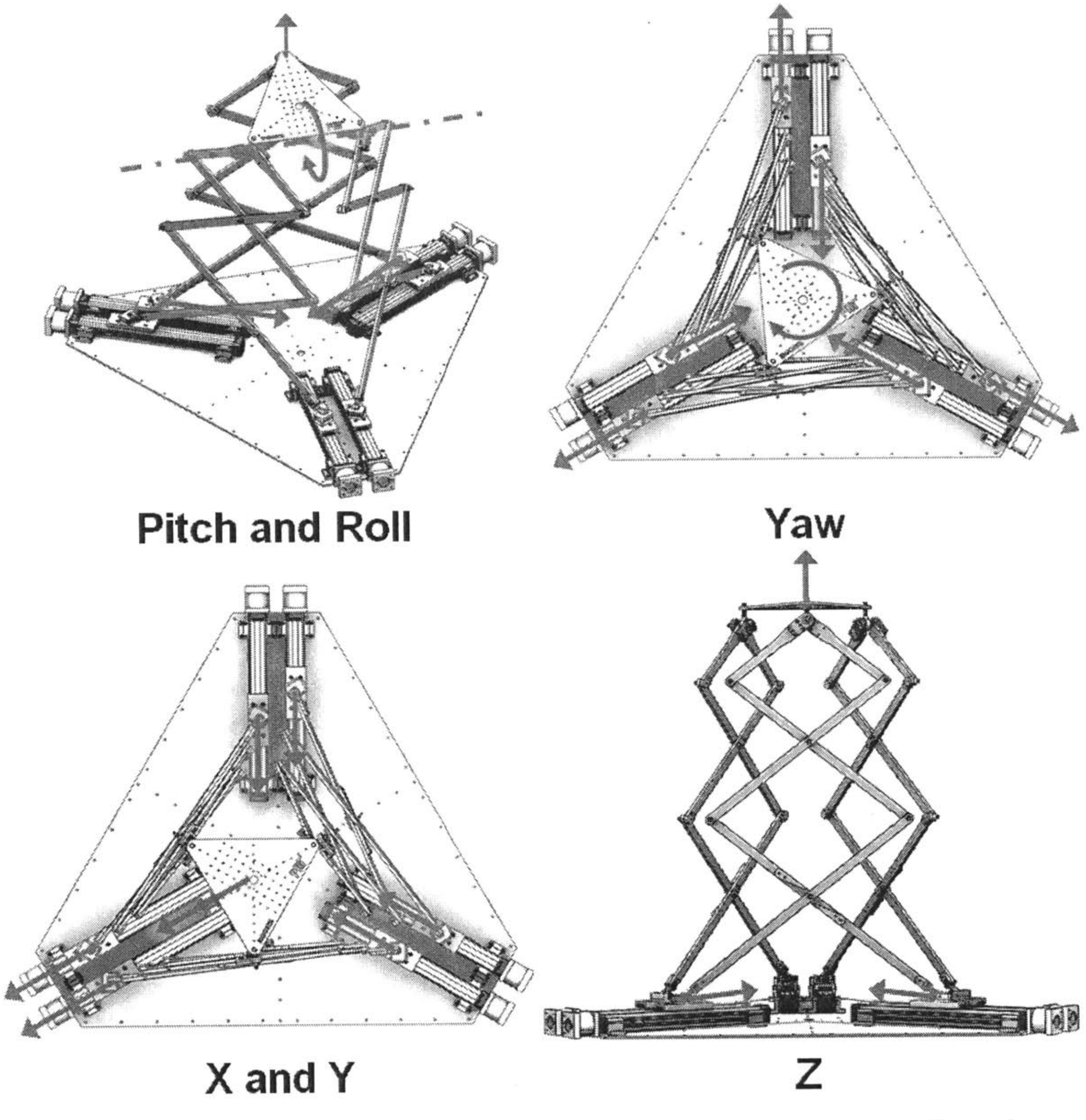
Pitch and Roll

Yaw

X and Y

Z

Figure 2-5: Intuitive Coordinated Motion Patterns of the Triple Scissor Extender

direction of motion.

By the coordinated superposition of these various modes of motion, the top platform can move to any desired pose within its workspace. Now that the geometry has been established, we may begin deriving the kinematic constraints.

Chapter 3

Modeling

3.1 Kinematics

3.1.1 The Inverse Kinematics Problem

Traditional 6-DOF platforms have relatively simple inverse kinematics solutions [4], but the highly coupled motion of the scissors relative to the actuators in the TSE make finding the inverse kinematics challenging. We now analyze the kinematic behavior of the TSE subject to geometric constraints and attain kinematic constraint equations.

Figure 3-1 shows the coordinate system used for describing the kinematic behavior of the Triple Scissor Extender. The top plate position is represented with vector $X_\epsilon^T = \begin{pmatrix} x_\epsilon & y_\epsilon & z_\epsilon \end{pmatrix}^T$ with reference to the base coordinate system $O - xyz$. The orientation of the top plate is described with roll, pitch, and yaw angles $\Theta = \begin{pmatrix} \varphi & \theta & \psi \end{pmatrix}^T$.

As shown in Figure 3-1, let $\hat{n}$, $\hat{t}$, $\hat{b}$ be, respectively, the unit vectors pointing in the three directions of a Cartesian coordinate frame $O_\epsilon - x'y'z'$ attached to the top plate. Concatenating these unit vectors in a 3x3 matrix we can write the orientation of the top plate in a compact expression

$$\begin{bmatrix} \hat{n} & \hat{t} & \hat{b} \end{bmatrix} = R_{xyz}(\varphi, \theta, \psi) = R_x(\varphi) R_y(\theta) R_z(\psi) \tag{3.1}$$

where $R_x(\varphi)$, $R_y(\theta)$, $R_z(\psi)$ are 3x3 rotation matrices about the x, y, and z axes,

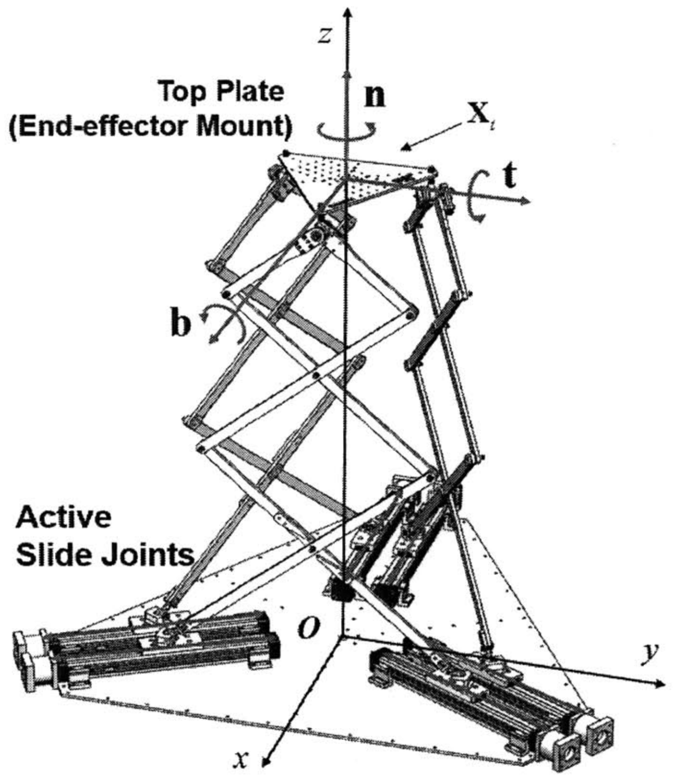

Figure 3-1: Base and end effectors coordinate systems

respectively.

The three apices of the top plate, C_1, C_2, and C_3, are connected to the three independent scissor mechanisms, while each scissor mechanism is activated with two linear actuators at the base. Let s_{Ai} and s_{Bi} be displacements of the linear actuators moving points A_i and B_i of the i-th scissor mechanism. Collectively, the six actuator displacements:

$$q = \begin{pmatrix} s_{A1} & s_{B1} & s_{A2} & s_{B2} & s_{A3} & s_{B3} \end{pmatrix}^T \tag{3.2}$$

form a 6-dimensional joint coordinate vector. These joint coordinates determine the top plate position and orientation:

$$p = \begin{pmatrix} X_\epsilon^T & \Theta_\epsilon^T \end{pmatrix}^T = \begin{pmatrix} x_\epsilon & y_\epsilon & z_\epsilon & \varphi_\epsilon & \theta_\epsilon & \psi_\epsilon \end{pmatrix}^T \tag{3.3}$$

The kinematic equation relating the endpoint pose p to the actuator displacements q is prohibitively complex, while its inverse kinematic relationship is tractable: $q = f(p)$.

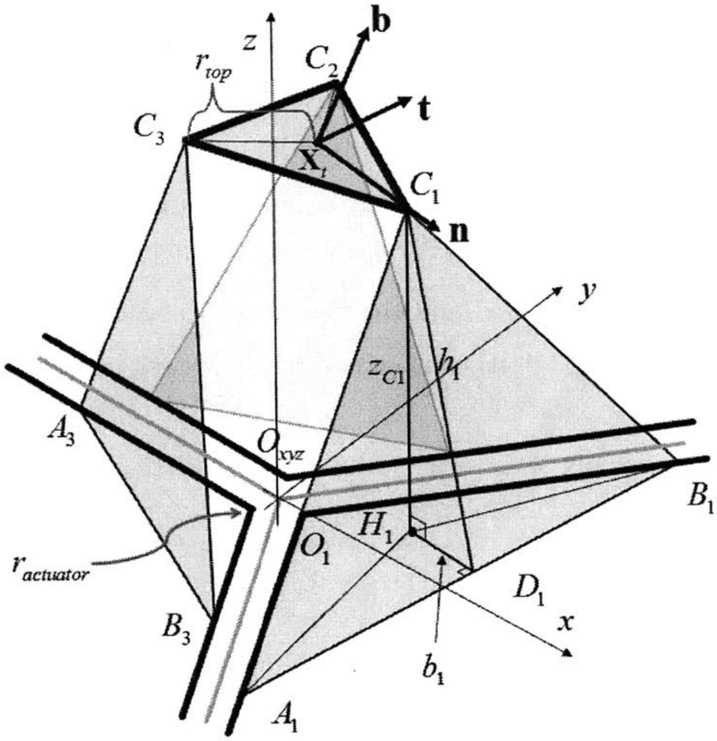
r_{top}
z
C_2
$\mathbf{b}$
$\mathbf{t}$
C_3
$\mathbf{X}_t$
C_1
$\mathbf{n}$
y
z_{C1}
h_1
A_3
O_{xyz}
B_1
$r_{actuator}$
H_1
O_1
D_1
x
B_3
b_1
A_1

Figure 3-2: Projection of Relevant Points onto the Base Plane

The Inverse Kinematics problem can be solved in the following steps:

- Given the 6-DOF pose p of the top plate, obtain coordinates of points C_1, C_2, and C_3 relative to the $O - xyz$ frame using the unit vectors in 3.1

$$\begin{aligned}
{}^{O}\vec{X}_{C1} &= {}^{O}\vec{X}_{top} + r_{top}\hat{n} \\
{}^{O}\vec{X}_{C2} &= {}^{O}\vec{X}_{top} + r_{top}\left(\frac{-1}{2}\hat{n} + \frac{\sqrt{3}}{2}\hat{t}\right) \\
{}^{O}\vec{X}_{C3} &= {}^{O}\vec{X}_{top} + r_{top}\left(\frac{-1}{2}\hat{n} - \frac{\sqrt{3}}{2}\hat{t}\right)
\end{aligned} \tag{3.4}$$

where r_{top} is the distance from the center of the top plate to each apex (See Figure 3-2).

- For each scissor mechanism i, given top point coordinates C_i, solve for the actuator displacements (s_{Ai}, s_{Bi}). In order to maintain generality, an intermediate coordinate system $O_i - xyz$ is created with its origin located at the intersection of linear slides A and B (See Figure 3-2), its $O_i - z$ axis parallel to the $O - z$ axis, and its y-axis pointing outward from the center of the TSE (see Figure3-4). The point coordinates of C_i are converted from the TSE origin frame $O - xyz$ to the new frame $O_i - xyz$, and the general Kinematic Constraint Equations derived in the next sections can be used to obtain the actuator displacements (s_{Ai}, s_{Bi})

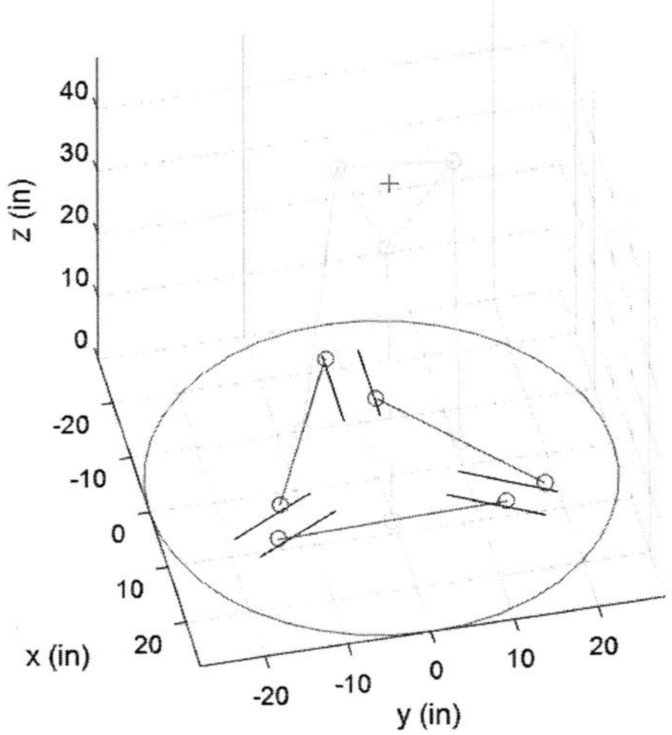

Figure 3-3: Inverse Kinematics being solved numerically in simulation

3.1.2 General Kinematic Constraint Derivation

2D Scissor Mechanism

Given the top points with respect to the origin O (3.4), define new coordinate systems with respect to scissor 1, scissor 2, and scissor 3.

$$\overline{O_0O_1} = \overline{O_0O_2} = \overline{O_0O_3} = r_{actuator} \tag{3.5}$$

$$^{i}\vec{X}_{Ci} = R_z\left(\alpha_i - \frac{\pi}{2}\right) {}^{O}\vec{X}_{Ci} - \begin{pmatrix} 0 & r_{actuator} & 0 \end{pmatrix}^T, \alpha = 0, \frac{2\pi}{3}, \frac{4\pi}{3} \tag{3.6}$$

First, the basic 2D kinematic relationship of a single scissor mechanism will be obtained. As shown in Figure 2-1, there is a functional relationship between the width of the scissors base, $w_i = \overline{A_iB_i}$, and the height of the scissors h_i, $i = 1, 2, 3$. For brevity, the subscript i will be omitted hereafter.

The scissor mechanism consists of n parallelograms of side length $\ell_1, \ell_2, \ldots, \ell_n$, and one isosceles triangle of equal side ℓ_0, connected at the center nodes $N_1, N_2, \ldots, N_n$. Let α be the angle of each scissor link relative to the baseline, $\alpha = \angle ABN_1$, as shown in the figure. The width w is given by

$$w = 2\ell_0 \cos(\alpha) \tag{3.7}$$

Since all the links are kept parallel, the height h is given by

$$h = L \sin(\alpha) \tag{3.8}$$

where the total length L is given by

$$L = \ell_0 + 2\ell_1 + \cdots + 2\ell_{n-1} + 2\ell_n \tag{3.9}$$

See Figure 2-1 for geometric interpretation. Eliminating angle α from (3.7) and (3.8) yields

$$\left(\frac{h}{L}\right)^2 + \left(\frac{w}{2\ell_0}\right)^2 = 1 \tag{3.10}$$

Projection onto the $O_1 - xy$ Plane

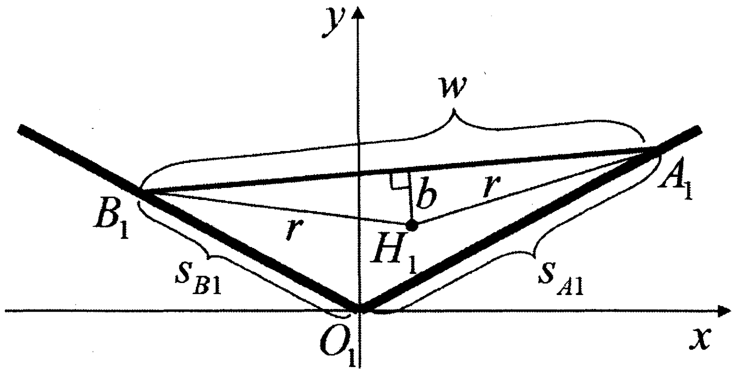

Figure 3-4: Top View of Base Plane showing Projected Point H on O_1xy-plane

As shown in Figure 3-2, consider the projection of Point C_1 onto the base plane, $O_1 - xy$. The projected point H_1 is redrawn within the $O_1 - xy$-plane in Figure 3-4. Again, for brevity, the subscript 1 is omitted in the following equations.

The (x, y) coordinates of scissor base points A and B are determined by the linear actuators, which move the scissors base points along the two radial directions, respectively. We must find the linear actuator coordinates ${}^ix_{Ai}$, ${}^iy_{Ai}$, ${}^ix_{Bi}$, ${}^iy_{Bi}$.

This is where the differences begin between each bottom platform configuration. The general Case of angle η up from the horizontal of O_i is:

$$\begin{aligned} {}^ix_{Ai} &= s_{Ai}\cos(\eta) \\ {}^iy_{Ai} &= s_{Ai}\sin(\eta) \\ {}^ix_{Bi} &= s_{Ai}\cos(\pi - \eta) \\ {}^iy_{Bi} &= s_{Ai}\sin(\pi - \eta) \end{aligned} \tag{3.11}$$

where $\eta = \pi/6$ corresponds to the Delta configuration, $\eta = 0$ for the Triangle configuration, $\eta = \pi/3$ for the Star60 configuration, and $\eta = -\pi/6$ for the Hexagonal configuration (See Figure 2-3). Therefore for the Delta configuration:

$$\begin{aligned} x_A &= s_A\cos\left(\frac{\pi}{6}\right), \quad y_A = s_A\sin\left(\frac{\pi}{6}\right) \\ x_B &= -s_B\cos\left(\frac{\pi}{6}\right), \quad y_B = s_B\sin\left(\frac{\pi}{6}\right) \end{aligned} \tag{3.12}$$

Using these coordinates, the width of the scissors, w, can be written as

$$w^2 = ({}^i x_{Ai} - {}^i x_{Bi})^2 + ({}^i y_{Ai} - {}^i y_{Bi})^2 \tag{3.13}$$

which, when combined with (3.12) simplifies to

$$w^2 = s_A^2 + s_B s_A + s_B^2 \tag{3.14}$$

for the Delta configuration.

Note that the scissor mechanism is symmetric with respect to its centerline connecting the center nodes $N_1, N_2, \ldots, N_n$. Therefore, point H_i, that is, the projection of point C onto the $O_i - xy$-plane, is on the bisector of the baseline AB. Hence, $\overline{AH} = \overline{BH} = r$, or

$$\begin{aligned} r^2 &= (x_A - x_C)^2 + (y_A - y_C)^2 \\ &= (x_B - x_C)^2 + (y_B - y_C)^2 \end{aligned} \tag{3.15}$$

where x_C and y_C are the xy coordinates of point C, i.e. those of point H. This produces two conditions for the Delta configuration

$$s_A^2 - \sqrt{3}(s_A + s_B)x_C = s_B^2 + (s_A - s_B)y_C \tag{3.16}$$

$$r^2 = s_A^2 - s_A(\sqrt{3}x_C + y_C) + x_C^2 + y_C^2 \tag{3.17}$$

(3.15) is the first Kinematic Constraint Equation.

Implicit equations relating apex coordinates (x_C, y_C, z_C) and actuator displacements (s_A, s_B)

The z coordinate of point C provides another condition by relating height of the scissor h_i to z_{Ci}. Consider the right triangle $C_1H_1D_1$ in Figure 3-2, where D is center point between s_A and s_B. We obtain

$$h^2 = b^2 + z_C^2 \tag{3.18}$$

where $b = \overline{HD}$.

By projecting the triangle on $O_i - xy$ plane as in Figure 3-4, we obtain

$$r^2 = b^2 + \left(\frac{w}{2}\right)^2 \tag{3.19}$$

Eliminate b^2 using equation (3.17):

$$h^2 - z_C^2 = r^2 - \left(\frac{w}{2}\right)^2 \tag{3.20}$$

Replace h^2 from scissor geometry equation (3.10):

$$L^2 - \frac{L^2 w^2}{4\ell_0^2} - z_C^2 = r^2 - \left(\frac{w}{2}\right)^2 \tag{3.21}$$

and rearrange:

$$r^2 + z_C^2 = L^2 + \frac{1}{4}\left(1 - \left(\frac{L}{\ell_0}\right)^2\right) w^2 \tag{3.22}$$

Replace w^2 using (3.12):

$$r^2 + z_C^2 = L^2 + \frac{1}{4}\left(1 - \left(\frac{L}{\ell_0}\right)^2\right) \left((x_A - x_B)^2 + (y_A - y_B)^2\right) \tag{3.23}$$

which, for the Delta configuration, becomes:

$$L^2 - \frac{L^2}{4\ell_0^2}(s_A^2 + s_B s_A + s_B^2) - z_C^2 = r^2 - \frac{1}{4}(s_A^2 + s_B s_A + s_B^2) \tag{3.24}$$

Replace r^2 by (3.15) to get Constraint Equation 2:

$$(x_A - x_C)^2 + (y_A - y_C)^2 + z_C^2 = L^2 + \frac{1}{4}\left(1 - \left(\frac{L}{\ell_0}\right)^2\right) \left((x_A - x_B)^2 + (y_A - y_B)^2\right) \tag{3.25}$$

For the Delta Configuration, this yields:

$$x_C^2 + y_C^2 + z_C^2 = L^2 - s_A^2 + s_A(\sqrt{3}x_C + y_C) + \frac{1}{4}\left(1 - \left(\frac{L}{\ell_0}\right)^2\right)(s_A^2 + s_B s_A + s_B^2) \tag{3.26}$$

Simultaneous equations (3.15) and (3.25) determine actuator displacements (s_A, s_B) for given coordinates (x_C, y_C, z_C). While the above derivation was only carried out for the first scissor mechanism, the other two scissor mechanisms can be treated in the same manner.

3.1.3 Nondimensionalized Kinematic Equations

In order to perform generic analysis of the kinematic properties of the TSE, the Kinematic Constraint Equations must be distilled to the most essential design parameters. We nondimensionalize equations (3.15) and (3.25) by scaling them by the total scissor length parameter L.

This leads to two new Kinematic Constraint Equations and four design parameters that define the entire design space for this class of machine:

- k_1: (ℓ_0/L), the ratio of the lowest scissor link length and the total scissor length L. See Figure 2-1.
- k_2: η, the angle of the actuator from the horizontal axis of its respective coordinate frame. See Figures 2-2 and 2-3.
- k_3: $(r_{actuator}/L)$, the ratio of the actuator coordinate frame radial distance from center and L. See Figures 2-2 and 2-4.
- k_4: (r_{top}/L), the ratio of the top platform distance to the ball joint and the total scissor length L. See Figure 2-4.

The scissor top points x_C, y_C, and z_C as well as the linear slide positions S_A and S_B are also normalized over the total scissor length L, which we define as $\hat{x_C}$, $\hat{y_C}$, $\hat{z_C}$, $\hat{S_A}$, and $\hat{S_B}$.

By rearranging and replacing variables in equations (3.15) and (3.25), the Non-Dimensionalized Kinematic Constraint Equations emerge:

$$\begin{aligned} \hat{S_A}^2 - 2\hat{x_C}\hat{S_A}\cos(k_2) + 2(k_3 - \hat{y_C})\hat{S_A}\sin(k_2) = \\ \hat{S_B}^2 - 2\hat{x_C}\hat{S_B}\cos(k_2) + 2(k_3 - \hat{y_C})\hat{S_B}\sin(k_2) \end{aligned} \tag{3.27}$$

and

$$\begin{aligned} \hat{S_A}^2 + 2(k_3 - \hat{y_C})\hat{S_A}\sin(k_2) + k_3^2 - 2\hat{y_C}k_3 + \hat{x_C}^2 + \hat{y_C}^2 + \hat{z_C}^2 = \\ 1 + 2\hat{x_C}\hat{S_A}\cos(k_2) + \frac{1}{4}\left(1 - \left(\frac{1}{k_1}\right)^2\right)\left(\hat{S_A}^2 + \hat{S_B}^2 + 2\hat{S_A}\hat{S_B}\cos(2k_2)\right) \end{aligned} \tag{3.28}$$

3.2 Formulation of the Inverse Jacobian

3.2.1 Characterizing the TSE Kinematic Properties

Based on the Inverse Kinematic relations obtained in the previous section, basic properties of the Triple Scissor Extender will be highlighted in this section through the analysis of differential motion.

Given a limited movable range, or stroke, of each actuator, "small workspace" implies a small end-effector displacement relative to large displacements at the actuators. In other words, the ratio of the end-effector displacement to the actuator displacements is small. Let $|\Delta q| = \sqrt{\Delta s_{A1}^2 + \Delta s_{A1}^2 + \cdots + \Delta s_{B3}^2}$ be the magnitude of the six actuator displacements, and $|\Delta X_\epsilon|$ and $|\Delta \Theta_\epsilon|$ be, respectively, the magnitude of the translational and rotational displacements of the end-effector. We characterize the kinematic properties of the TSE in terms of the ratios:

$$\gamma_t(p) = \frac{|\Delta X_\epsilon|}{\Delta q}, \gamma_r(p) = \frac{|\Delta \Theta_\epsilon|}{\Delta q}, a \tag{3.29}$$

which physically mean spatial, multi-DOF "gear ratios" associated with the translation and rotation of the end-effector, respectively. These ratios vary depending on the end-effector pose p, as well as the direction of the end-effector motion. We will obtain the maximum and the minimum of $\gamma_t(p)$ and $\gamma_r(p)$ at each configuration of the end-effector pose p, and examine how the maximum/minimum ratios distribute over the workspace.

This entails identifying the Jacobian relating the end-effector displacements to actuator displacements

$$\Delta q = \mathbb{J}_I \Delta p \tag{3.30}$$

where $\mathbb{J}_I$ is the 6×6 Inverse Jacobian matrix. This is also often called the Manipulability Matrix [6]. Note that the elements of the Jacobian Matrix are partial derivatives of input motion to output motion, not time derivatives.

As in the previous kinematic analysis, the Inverse Jacobian Matrix can be split into two main parts. We obtain the differential relationship

$$(\Delta C_1 \quad \Delta C_2 \quad \Delta C_3)^T = \mathbb{J}_C \Delta \vec{p} \tag{3.31}$$

where $\mathbb{J}_C$ is the 9×6 Jacobian between the top platform pose $\vec{p}$ and the top platform apexes C_i. For top platform translation, differential motion is 1:1, and the left half of $\mathbb{J}_C$ is made of Identity matrices. For top platform rotation, which corresponds with the right half of $\mathbb{J}_C$, the differential motion can be obtained from the transform matrices of (3.1).

For each scissor we obtain the differential relationship between point C_i and actuator displacements s_A and s_B where

$$\mathbb{J}_{S_i} = \begin{bmatrix} \dfrac{\partial s_{Ai}}{\partial x_{Ci}} & \dfrac{\partial s_{Ai}}{\partial y_{Ci}} & \dfrac{\partial s_{Ai}}{\partial z_{Ci}} \\ \dfrac{\partial s_{Bi}}{\partial x_{Ci}} & \dfrac{\partial s_{Bi}}{\partial y_{Ci}} & \dfrac{\partial s_{Bi}}{\partial z_{Ci}} \end{bmatrix} \tag{3.32}$$

is the individual scissor Jacobian and the block matrix

$$\mathbb{J}_S = \begin{bmatrix} \mathbb{J}_{S1} & 0 & 0 \\ 0 & \mathbb{J}_{S2} & 0 \\ 0 & 0 & \mathbb{J}_{S3} \end{bmatrix} \tag{3.33}$$

is the combined 6 × 9 scissor Jacobian.

When both $\mathbb{J}_C$ and $\mathbb{J}_S$ combined, we obtain

$$\mathbb{J}_I = \mathbb{J}_S \mathbb{J}_C \tag{3.34}$$

which is the final 6 × 6 Inverse Jacobian Matrix.

Obtaining $\mathbb{J}_S$ typically requires the Inverse Kinematics, which is not explicitly solvable. In the following sections the outline of an alternative computation of $\mathbb{J}_S$ is described.

3.2.2 Computation of the Jacobians

TSE consists of three pairs of scissor mechanisms, each governed by the implicit kinematic equations (3.15) and (3.25). These determine the relationship between actuator displacements s_A, s_B and the apex position x_C, y_C, z_C in the local coordinate frame $O_i - x_i y_i z_i$. For brevity the subscript is again omitted. Differentiating both equations (3.15) and (3.25) at a given apex position p, we can obtain a differential relationship in the following form:

$$\begin{aligned} a_{11}\Delta s_A + a_{12}\Delta s_B &= b_{11}\Delta x_c + b_{12}\Delta y_c + b_{13}\Delta z_c \\ a_{21}\Delta s_A + a_{22}\Delta s_B &= b_{21}\Delta x_c + b_{22}\Delta y_c + b_{23}\Delta z_c \end{aligned} \tag{3.35}$$

where parameters $a_{11}, \ldots, b_{23}$ are evaluated at the given apex position $\vec{p}$. Using vector-matrix form, we can write the Jacobian relating the two actuator displacement Δs_A, Δs_B to those of the apex coordinates Δx_C, Δy_C, Δz_C as:

$$\begin{pmatrix} \Delta s_A \\ \Delta s_B \end{pmatrix} = \mathbb{J}_S \Delta \mathbf{X}_c, \quad \Delta \mathbf{X}_c = \begin{pmatrix} \Delta x_c \\ \Delta y_c \\ \Delta z_c \end{pmatrix} \tag{3.36}$$

where $\mathbb{J}_S = \mathbf{A}^{-1}\mathbf{B},\ \mathbf{A} = \{a_{ij}\}, \mathbf{B} = \{b_{ij}\}$. Of particular interest is the case where the top plate is kept level and moves along the z-axis. At this center configuration, $s_A = s_B = s$ and $x_c = 0,\ y_c = \ell_t - \Delta\gamma$ (where γ is half the distance between adjacent linear slides such as s_{B1} and s_{A2}), the Jacobian is given by

$$\mathbb{J}_S\,|_{Center} = \begin{pmatrix} \dfrac{\sqrt{3}s}{2s - \ell_t + \Delta\gamma} & -\dfrac{\sqrt{3}s}{2s - \ell_t + \Delta\gamma} \\ \dfrac{2(\ell_t - \Delta\gamma) - s}{6cs - 2s + \ell_t - \Delta\gamma} & \dfrac{2(\ell_t - \Delta\gamma) - s}{6cs - 2s + \ell_t - \Delta\gamma} \\ \dfrac{2z_c}{6cs - 2s + \ell_t - \Delta\gamma} & \dfrac{2z_c}{6cs - 2s + \ell_t - \Delta\gamma} \end{pmatrix}^T \tag{3.37}$$

which is a specific version of the general Jacobian in (3.32).

We can obtain similar equations for all three scissor mechanisms. We denote the three Jacobians by $\mathbb{J}_{S1}, \mathbb{J}_{S2}, \mathbb{J}_{S3}$.

The apex local coordinates are functions of the end-effector position and orientation, $\mathbf{X}_\epsilon$ and Θ_ϵ, according to (3.25). For the first pair of scissors, its derivatives are given by

$$\Delta\mathbf{X}_{C1} = \Delta\mathbf{X}_\epsilon + \ell_t \frac{d\hat{\mathbf{n}}}{d\Theta_\epsilon} \Delta\Theta_\epsilon \tag{3.38}$$

Substituting (3.39) in (3.36) yields

$$\begin{pmatrix} \Delta s_{A1} \\ \Delta s_{B1} \end{pmatrix} = \mathbb{J}_{S1} \Delta\mathbf{X}_\epsilon + \ell_t \mathbb{J}_{S1} \frac{d\hat{\mathbf{n}}}{d\Theta_\epsilon} \Delta\Theta_\epsilon \tag{3.39}$$

Similarly for the other two pairs of scissor mechanisms,

$$\begin{aligned} \begin{pmatrix} \Delta s_{A2} \\ \Delta s_{B2} \end{pmatrix} &= \mathbb{J}_{S2} \Delta\mathbf{X}_\epsilon - \ell_t \mathbb{J}_{S2} \left(\frac{\sqrt{3}}{2} \frac{d\hat{\mathbf{t}}}{d\Theta_\epsilon} + \frac{1}{2} \frac{d\hat{\mathbf{n}}}{d\Theta_\epsilon} \right) \Delta\Theta_\epsilon \\ \begin{pmatrix} \Delta s_{A3} \\ \Delta s_{B3} \end{pmatrix} &= \mathbb{J}_{S3} \Delta\mathbf{X}_\epsilon + \ell_t \mathbb{J}_{S3} \left(\frac{\sqrt{3}}{2} \frac{d\hat{\mathbf{t}}}{d\Theta_\epsilon} - \frac{1}{2} \frac{d\hat{\mathbf{n}}}{d\Theta_\epsilon} \right) \Delta\Theta_\epsilon \end{aligned} \tag{3.40}$$

From (3.1) the derivatives of the unit vectors at the centerline are given by

$$\frac{d\hat{\mathbf{t}}}{d\Theta_\epsilon} = \begin{pmatrix} 0 & 0 & 0 \\ 0 & 0 & 1 \\ 0 & -1 & 0 \end{pmatrix}, \quad \frac{d\hat{\mathbf{n}}}{d\Theta_\epsilon} = \begin{pmatrix} 0 & 0 & -1 \\ 0 & 0 & 0 \\ 1 & 0 & 0 \end{pmatrix} \tag{3.41}$$

Combining these yields,

$$\Delta\mathbf{q} = \mathbb{J}_t \Delta\mathbf{X}_\epsilon + \mathbb{J}_r \Delta\Theta_\epsilon \tag{3.42}$$

where

$$\mathbb{J}_t = \begin{pmatrix} \mathbb{J}_{S1} \\ \mathbb{J}_{S2} \\ \mathbb{J}_{S3} \end{pmatrix} \in \Re^{6\times 3} \tag{3.43}$$

is the Jacobian associated with the translational displacement of the end-effector, and

$$\mathbb{J}_r = \ell_t \begin{pmatrix} \mathbb{J}_{S1} \dfrac{d\hat{\mathbf{n}}}{d\Theta_\epsilon} \\ -\mathbb{J}_{S2} \left(\dfrac{\sqrt{3}}{2} \dfrac{d\hat{\mathbf{t}}}{d\Theta_\epsilon} + \dfrac{1}{2} \dfrac{d\hat{\mathbf{n}}}{d\Theta_\epsilon} \right) \\ \mathbb{J}_{S3} \left(\dfrac{\sqrt{3}}{2} \dfrac{d\hat{\mathbf{t}}}{d\Theta_\epsilon} - \dfrac{1}{2} \dfrac{d\hat{\mathbf{n}}}{d\Theta_\epsilon} \right) \end{pmatrix} \in \Re^{6\times 3} \tag{3.44}$$

is the Jacobian associated with the rotational displacement of the end-effector. From these we can obtain the block matrices (3.33) and (3.34), and thus the full Inverse Jacobian Matrix about this specific center point.

Chapter 4

Analysis

4.1 Differential Motion and Manipulability Analysis through Spatial Gear Ratios

The maximum of the translational gear ratio $\gamma_t(\mathbf{p}) = |\Delta \mathbf{X}_e| \,/\, |\Delta \mathbf{q}|$ is given by the minimum non-zero singular value associated with the Singular-Value Decomposition [5] of Jacobian $\mathbb{J}_t$, (and vice-versa for the maximum gear ratio):

$$\mathbb{J}_t = \mathbf{U}_t \Sigma_t \mathbf{V}_t^T \tag{4.1}$$

where $\Sigma_t \in \Re^{6\times 3}$ is a rectangular diagonal matrix consisting of the square root of the eigenvalues associated with the real symmetric matrix $\mathbb{J}_t^T \mathbb{J}_t \in \Re^{3\times 3}$:

$$\Sigma_t = \begin{pmatrix} 1/\lambda_{t1} & 0 & 0 \\ 0 & 1/\lambda_{t2} & 0 \\ 0 & 0 & 1/\lambda_{t3} \\ 0 & 0 & 0 \\ 0 & 0 & 0 \\ 0 & 0 & 0 \end{pmatrix} \tag{4.2}$$

$$(0 < \lambda_{t1} \le \lambda_{t2} \le \lambda_{t3})$$

and $\mathbf{U}_t \in \Re^{6\times6}$ and $\mathbf{V}_t \in \Re^{3\times3}$ are, respectively, unitary matrices consisting of the eigenvectors of the matrices $\mathbb{J}_t\mathbb{J}_t^T \in \Re^{6\times6}$ and $\mathbb{J}_t^T\mathbb{J}_t \in \Re^{3\times3}$. Note that the Jacobian matrices we have obtained are for the *inverse* kinematics relating actuator displacements to the end-effector displacements, thus taking the reciprocal of the eigenvalue in (30). The rotational gear ratio $\gamma_r(\mathbf{p}) = |\Delta\Theta_e| \,/\, |\Delta\mathbf{q}|$can be examined in a similar manner.

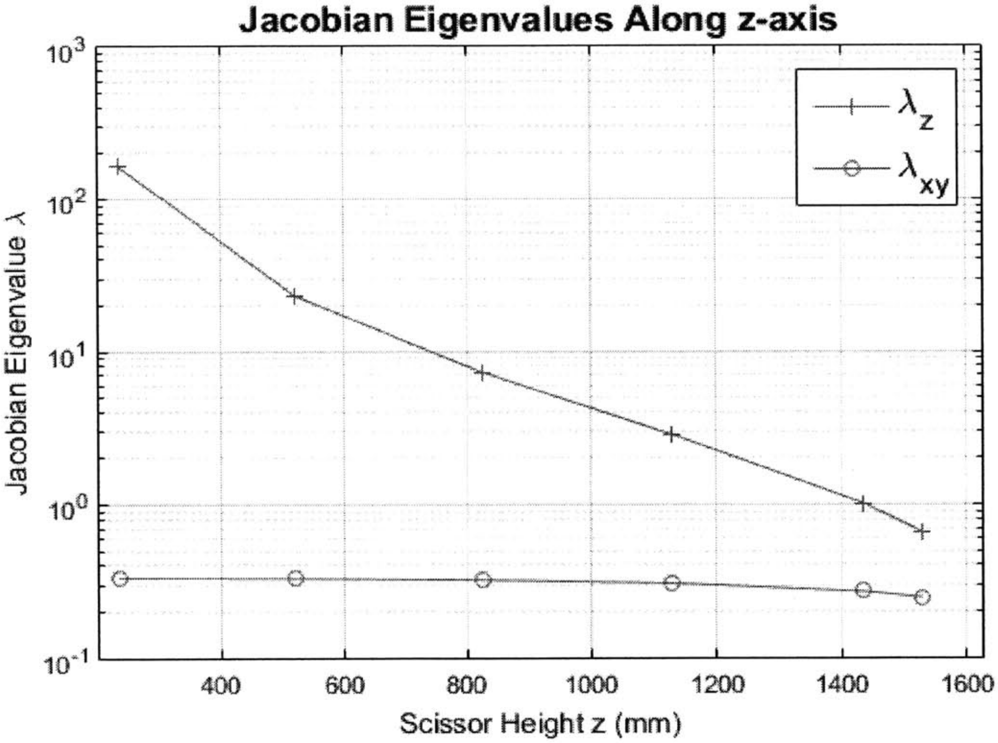

Figure 4-1: Jacobian at Various Heights along z-axis

Figures 4-1 and 4-2 show the translational gear ratio $\gamma_t(\mathbf{p}) = |\Delta\mathbf{X}_e| \,/\, |\Delta\mathbf{q}|$ at diverse end-effector locations along the z-axis. Note that near the ground the vertical component of γ_t grows large, and as the top platform nears the end of its upward travel γ_t decreases, indicating a singular configuration where no more upward motion can be obtained. This can be interpreted intuitively by thinking of the three scissor mechanisms as the TSE top platform moves upward and how they elongate until no more motion can be achieved.

Figure 4-3 shows the translational gear ratio γ_t for various points at a constant

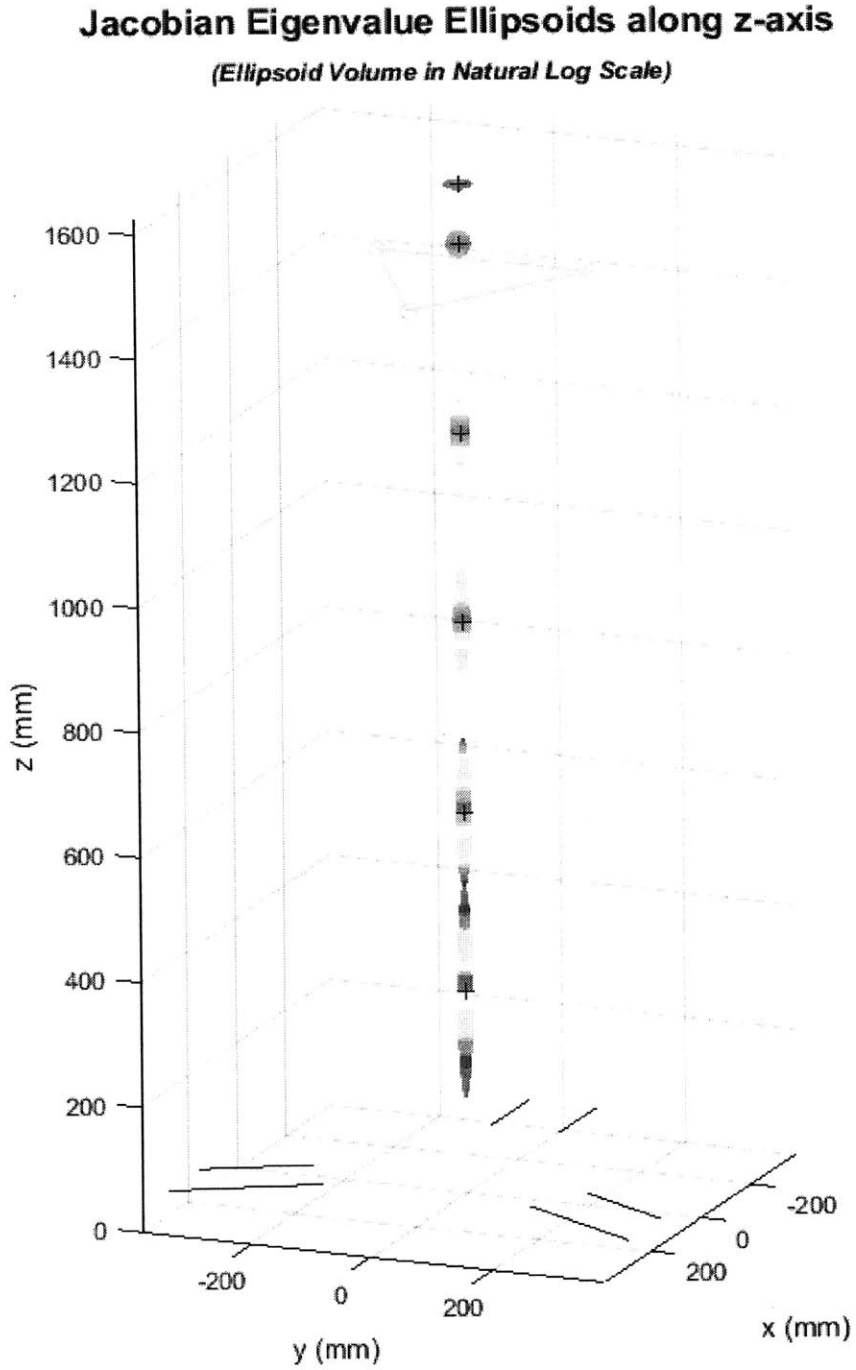

Figure 4-2: Jacobian Ellipsoids for points along z-axis.

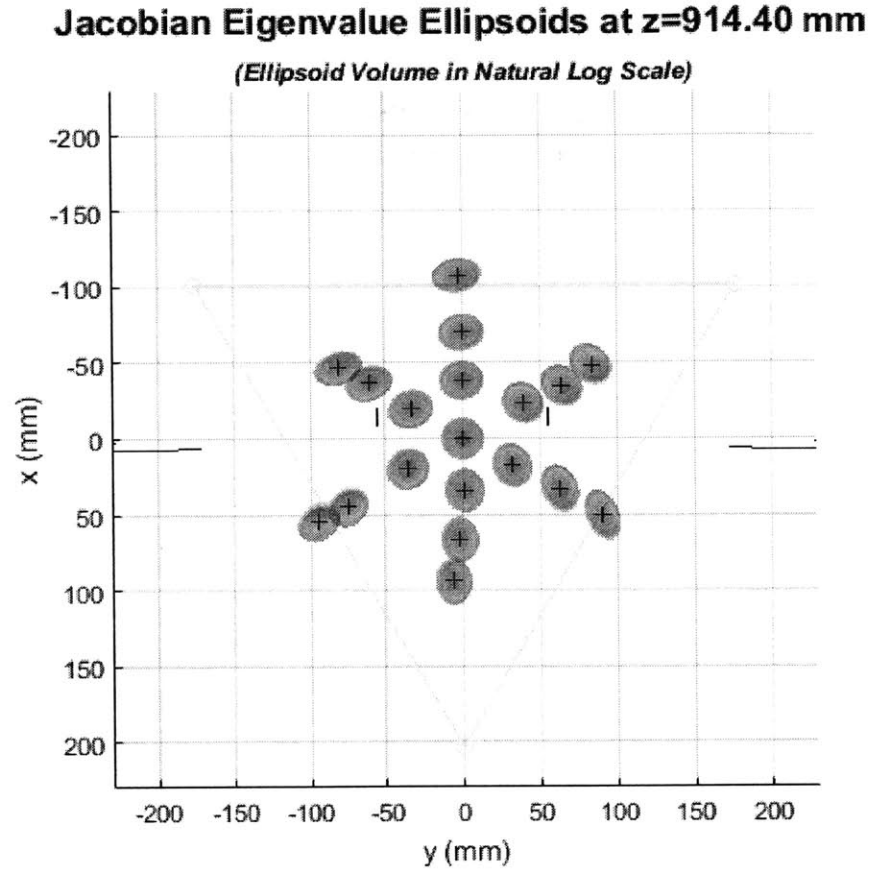

Figure 4-3: Jacobian Ellipsoids for points at constant $z = 914.40$ millimeters

height in the center of the TSE's workspace. While virtual gear ratio values along the x and y axes do change as a function of the robot's configuration, they do not change as dramatically as the virtual gear ratio in the vertical direction does. This difference between the planar and vertical components of γ_t serves to further highlight the nature of the TSE, which was designed with vertical motion amplification in mind. This result serves to mathematically validate our design.

4.2 Design Parameter Sensitivity Analysis

In Section 3.1.3, the Nondimensionalized Kinematic Constraint Equations (3.15) and (3.25) were derived in order to facilitate the analysis of the kinematic properties of the TSE. In this section, we analyze how changing the kinematic design parameters

k_1, k_2, and k_3 affect the configuration-dependent Translational Spatial Gear Ratios of the TSE.

Note that k_4 does not appear in the Kinematic Constraint Equations, but only in the first step of the Inverse Kinematics problem, where the apex points C_i are found. k_4 affects the *Rotational* Spatial Gear Ratio, which are not analyzed for brevity.

For these analyses, the design parameters chosen match those of the implemented prototype from Chapter 5 and a single design parameter was deviated from this value to determine how it affects the Spatial Gear Ratios, the Jacobian Eigenvalues.

4.2.1 Sensitivity due to scissor length ratio k_1

The scissor length ratio k_1 carries with it the essence of the Triple Scissor Extender: height amplification using scissor mechanisms. The value k_1 can be thought of intuitively as the height amplification factor.

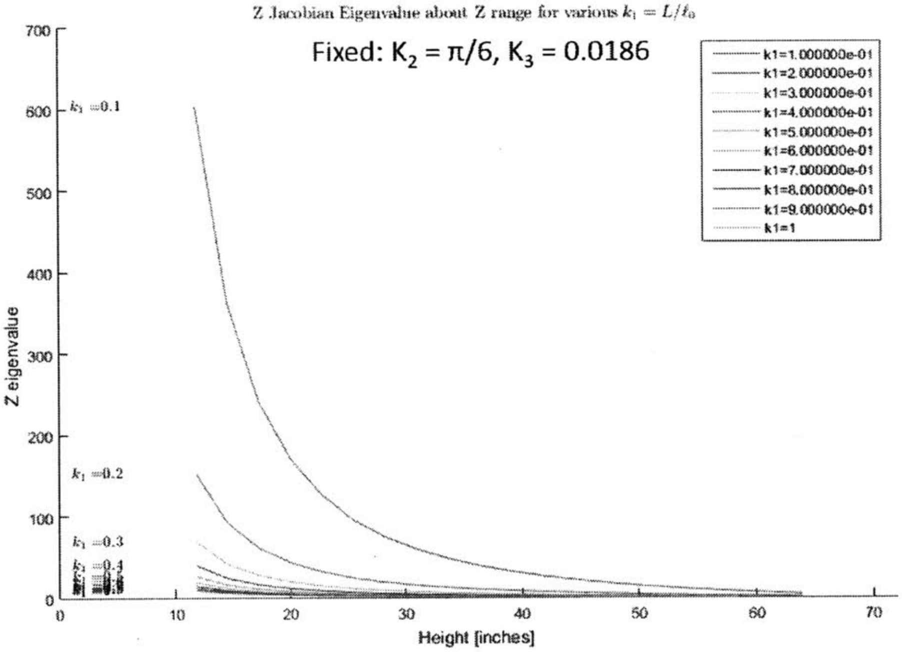

Figure 4-4: Jacobian Eigenvalues with Changing Length Ratio

As can be seen in Figure 4-4. the lower the value of k_1, the greater the sensitivity to motion, or height amplification factor.

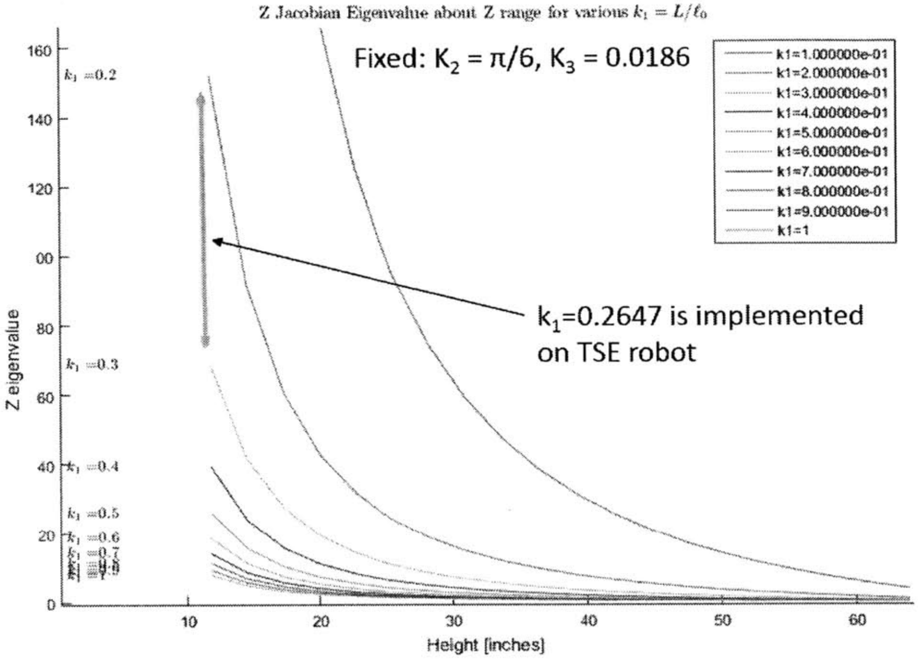

Figure 4-5: Jacobian Eigenvalues with Changing Length Ratio (Zoomed In Near k_1 of Prototype)

The implemented Prototype has a k_1 of 0.2647, which leads to a maximum Z Jacobian Eigenvalue of nearly 110, as can be seen in Figure 4-5. This follows with the results shown in Figure 4-1.

A $k_1 = 1$ has an equal total scissor length and lowest length, $L = \ell_0$, which has no scissor at all. This configuration of the TSE is identical to many other Hexapod platforms with rigid links and stationary linear actuators at the base, and has no amplification factor, as can be seen in Figure 4-6.

4.2.2 Sensitivity due to Actuator Angle k_2

Intuitively, by changing the scissor angle k_2, we affect the rate of change of the width between the bottom points of the scissors, which directly affects the Z Jacobian Eigenvalue. Collinear slides, where $k_2 = 0°$ will have the largest Z Jacobian Eigenvalue, and any deviation from this will decrease this value.

As shown in Figure 4-7, with a k_1 or 0.2647, TSE configurations with $k_2 < 45°$ are

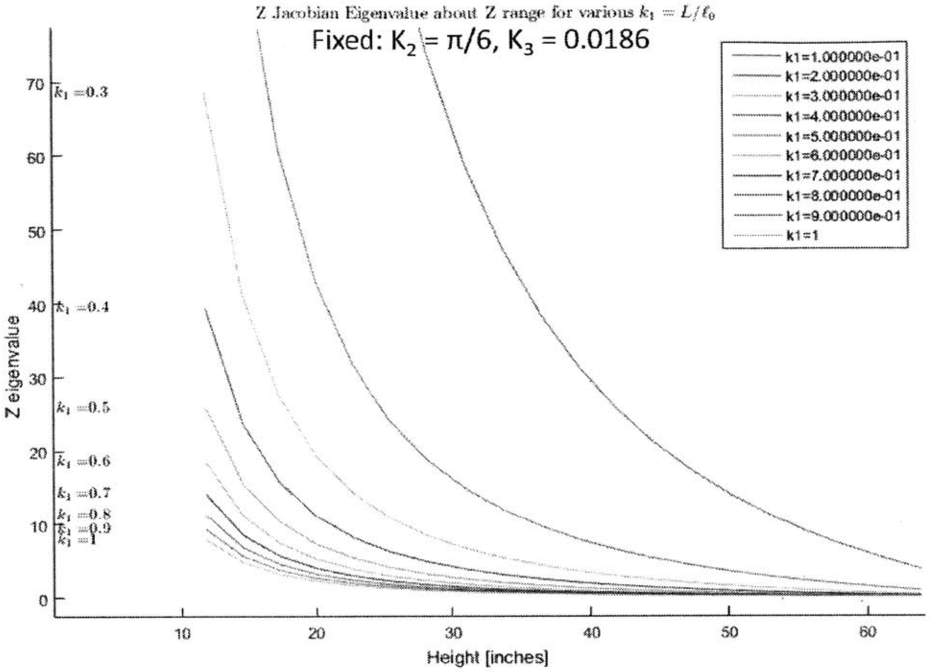

Figure 4-6: Jacobian Eigenvalues with Changing Length Ratio (Zoomed In Near $k_1 = 1$)

valid, and the Z Eigenvalue range scales with changing $k2$. All configurations with $k_2 > 45°$, however, exhibit behaviors consistent with singular configurations.

This strange behavior is more evident in Figure 4-8, which shows the Jacobian Eigenvalues on a log scale. For some negative k_2, there is a critical range of k_1 where the scissor bottom points are moving away nearly as fast as the scissor mechanism extends.

We explore the possibility of having a negative slide angle k_2 by choosing a different k_1.

As shown in Figure 4-9 a lower amplification ratio (higher k_1), angles of k_2 higher than 45° are valid. Positive and negative values of the angle, while significantly changing the appearance of the TSE, exhibit similar behavior in the z-direction.

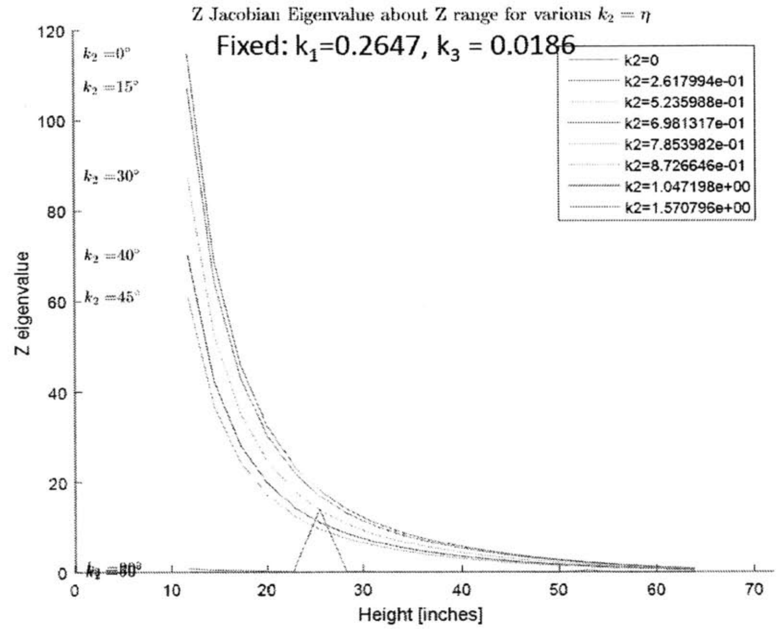

Figure 4-7: Jacobian Eigenvalues with changing Slide Angle

4.2.3 Sensitivity due to Actuator Coordinate Radius k_3

The Z Jacobian Eigenvalues do not change significantly for differing values of k_3, as can be shown in Figure 4-10. They scale linearly with k_3, but the shape is mostly unchanged.

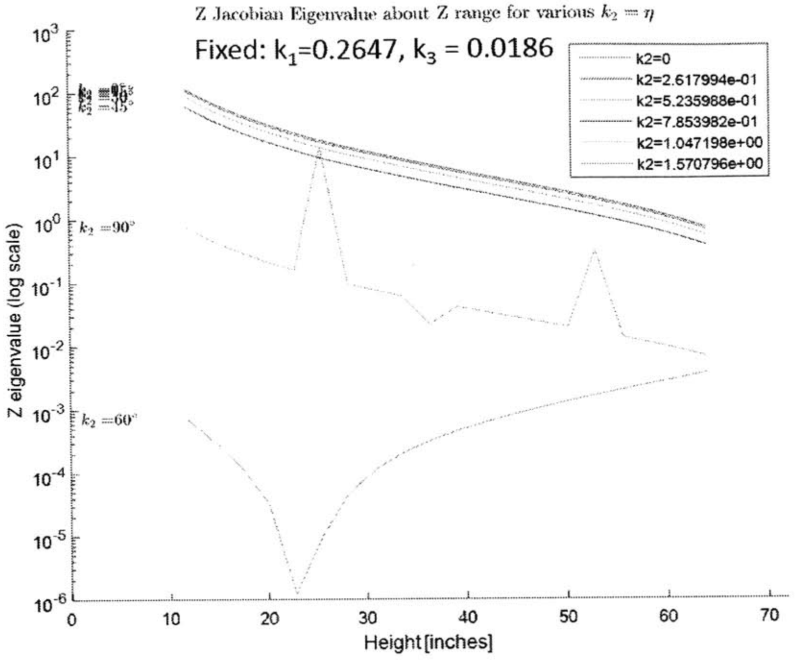

Figure 4-8: Jacobian Eigenvalues with changing Slide Angle (Log Scale)

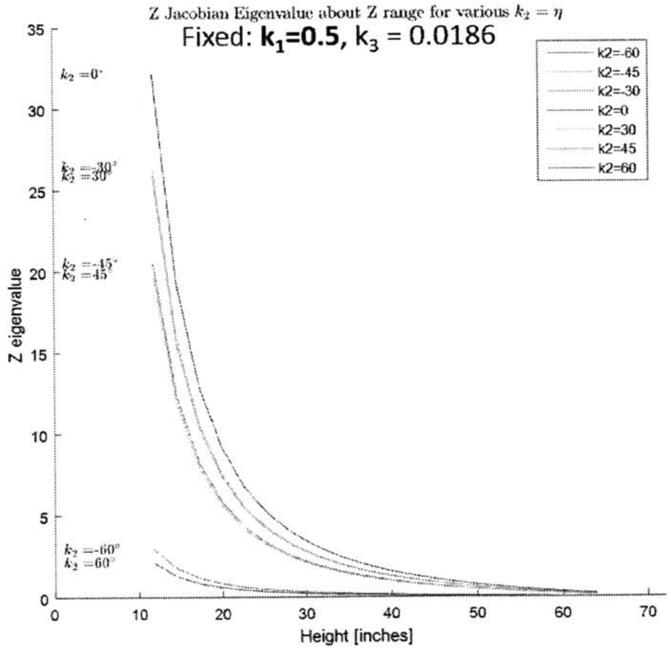

Figure 4-9: Jacobian Eigenvalues with changing Slide Angle for larger k_1

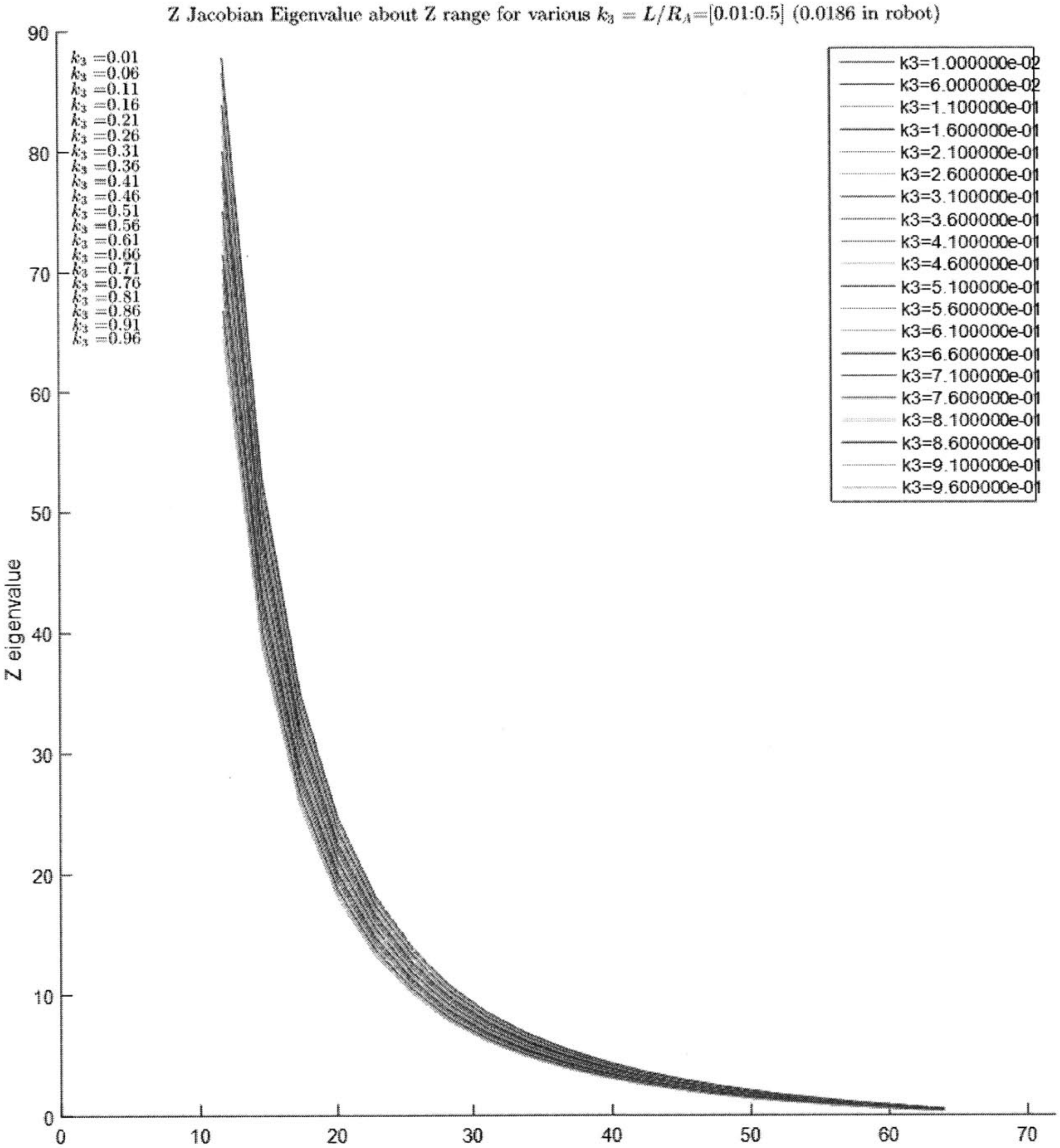

Figure 4-10: Jacobian Eigenvalues with changing Actuator Coordinate System Radius

Chapter 5

Detailed Design of Prototype

A prototype Triple Scissor Extender (TSE) was built to test our kinematic model. The size of the robot was chosen such that it would have a maximum height of 1619.25 millimeters (63.75 inches) while being able to collapse to a height of 323.85mm (12.75 inches). The ratio between the lowest link length and the total length, ℓ_0/L, is 0.0247. This allows for a maximum height amplification of 5. The TSE was designed to meet certain functional requirements.

The functional requirements of the Triple Scissor Extender are as follows:

- The Triple Scissor Extender Prototype must demonstrate all modes of motion.
- It must be short enough to be easily transported (12.75 inches).
- It must be as tall as a person at its highest configuration (63.75 inches).
- It must bear an external 25 lb load at the top platform in addition to the gravitational loading of the TSE structure itself, assumed to be 25 lbs. (50lbs total)
- It must move from its shortest configuration to its tallest in no more than 5 seconds.
- It must have standard 1/4-20 1-inch-by-1-inch breadboard grid pattern mounting features at the top platform for multi end-effector mounting.

- It must be designed and built quickly in order to demonstrate to sponsors as soon as possible.
    - There were 2 months and 12 days from the original conception to sponsor demonstration.
    - Design for easy manufacturing and assembly, and use commercial off-the-shelf (COTS) parts when possible.
- It must be designed with future upgrades to structure, actuation, control hardware and control software, particularly with regards to autonomy, in mind.
- It must be easily movable in order to relocate it while in the laboratory.

5.1 Static Loading Analysis and Actuator Specifications

In order to quickly prototype the Triple Scissor Extender, the most critical components, the six linear actuators located at the base, were purchased as COTS parts. In order to keep costs down and demonstrate the motion of the TSE, the actuators were chosen for only strength, not stiffness.

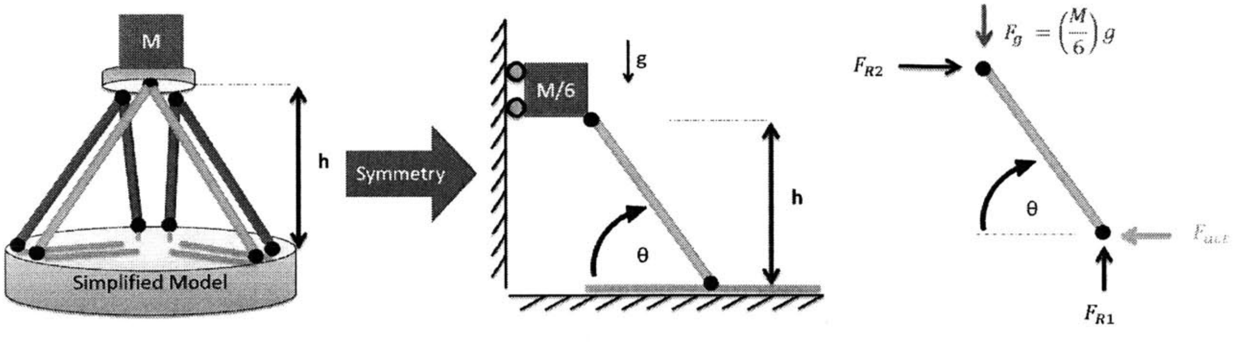

Figure 5-1: Simplified models and Free Body Diagram of the Triple Scissor Extender worst-case loading situations.

The linear carriages, ballscrew assemblies, servo motors, and servo drives were chosen by analyzing the worst-case loading while bearing a 11.34 kilogram (25 pound) external payload. The stroke, max speed, structural load-bearing capacity of the carriage, and force output capability of the actuators were all considered.

In order to sufficiently model the worst-case loading of the Triple Scissor Extender, a simplified model that captured the loading cases of the linear actuator was developed (Figure 5-1). Due to symmetry, a 1-DOF case of actuator loading is all that needs to be considered for actuator specification.

Figure 5-1 also shows a Free Body Diagram of this 1-DOF representation of worst-case actuator loading. The static equations governing the forces that must be borne by the actuators are:

$$F_{actuator} = F_g \cot\theta = \left(\frac{M}{6}\right) g \cot\theta \tag{5.1}$$

$$F_{R1} = F_g = \left(\frac{M}{6}\right) g \tag{5.2}$$

$$F_{R2} = F_{actuator} \tag{5.3}$$

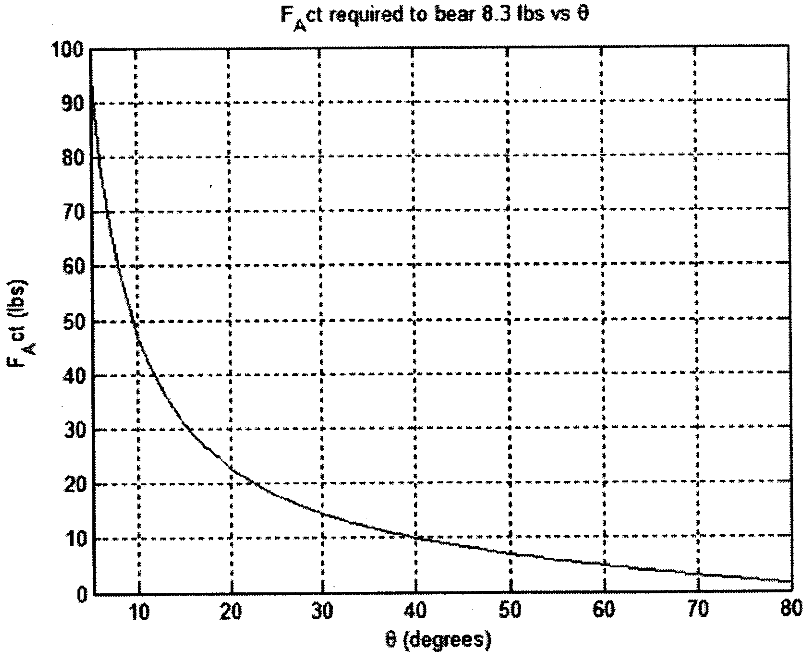

Figure 5-2: Individual actuator force F_{act} required to bear a total load of 50 pounds at a given angle θ

Figure 5-2 shows (5.1) for changing θ. The actuator force F_{act} approaches ∞ as the TSE nears a singular configuration where $\theta = 0°$. The force approaches 0 as the TSE moves to the singularity near its highest configuration $\theta = 90°$, where no force is required from the actuation to bear the load. The actuators were chosen to handle a lowest configuration of $\theta = 5°$, each actuator must provide 95.45 pounds of force to bear the total 50 pound load of the TSE and payload.

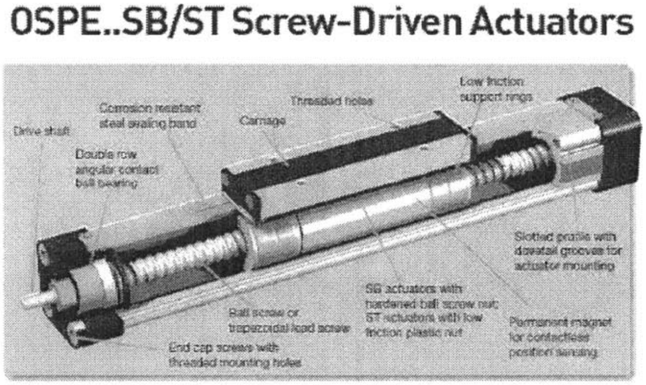
OSPE..SB/ST Screw-Driven Actuators
Drive shaft
Corrosion resistant steel sealing band
Carriage
Threaded holes
Low friction support rings
Double row angular contact ball bearing
Slotted profile with dovetail grooves for actuator mounting
SB actuators with hardened ball screw nut; ST actuators with low friction plastic nut
Ball screw or trapezoidal lead screw
Permanent magnet for contactless position sensing
End cap screws with threaded mounting holes

Figure 5-3: Section view of the Parker OSPE 32 SB Actuator

Parker Origa OSPE 32 SB actuators (Figure 5-3) with a 300 millimeter stroke were chosen as the main actuators for the TSE Prototype. In order to allow for high efficiency low-impedance backdrivability, 5 millimeter pitch ballscrew drives were chosen with brushless servo motors.

5.2 Structure, Joint, and Linkage Design

With the main actuators chosen, the rest of the structure was designed to meet the functional requirements. The overall structural geometry, the strength of each link and joint of each scissor mechanism, and the interfacing between each part of the assembly, were all considered.

Figure 5-4 shows a single scissor mechanism. The individual link lengths were chosen such that the TSE could never be configured such that the two scissors could intersect. Each scissor mechanism is attached at the bottom points A and B as well

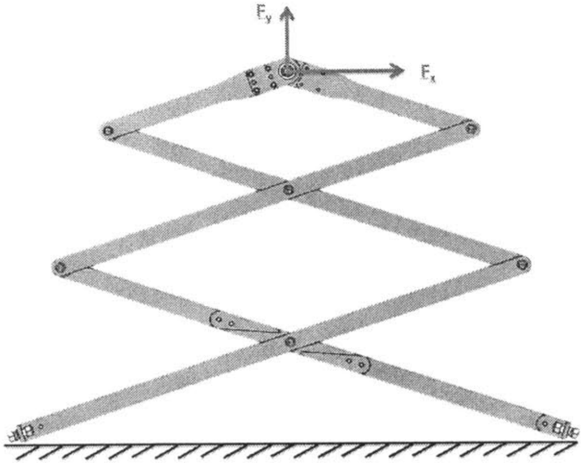

Figure 5-4: A single scissor mechanism, and the forces it must bear.

as the top point C by commercial off-the-shelf ball joint rod ends. The geometry was designed with hard stops such that the TSE would never pass through a singular configuration.

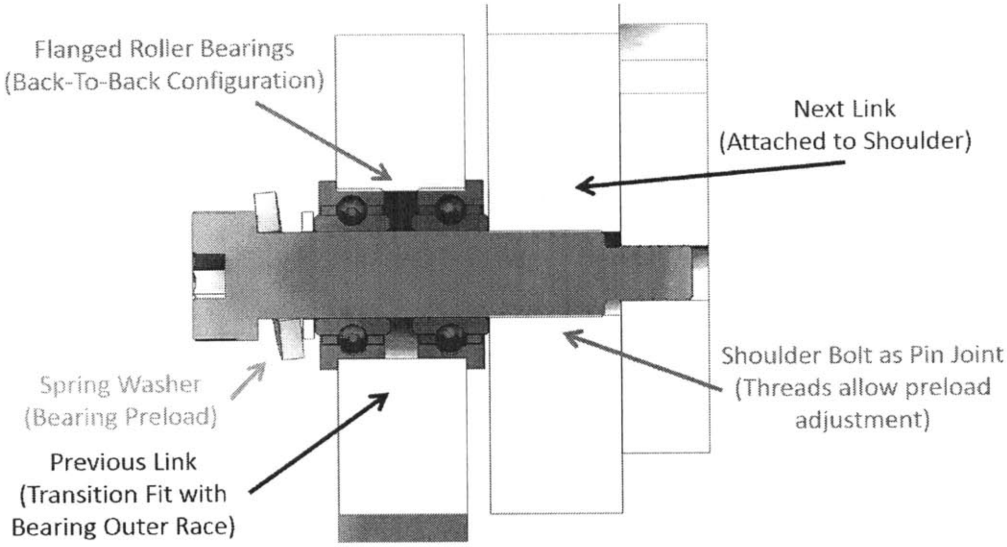
Flanged Roller Bearings
(Back-To-Back Configuration)
Next Link
(Attached to Shoulder)
Spring Washer
(Bearing Preload)
Shoulder Bolt as Pin Joint
(Threads allow preload adjustment)
Previous Link
(Transition Fit with Bearing Outer Race)

Figure 5-5: Section view of a single joint of the TSE scissor linkages.

Each joint uses twin flanged roller bearings in a back-to-back configuration, shown in Figure 5-5. The bearings are preloaded for stiffness with a spring washer, and a shoulder bolt is used as a shaft.

The top ball joints (Figure 5-6) were chosen to maximize the pitching/rolling

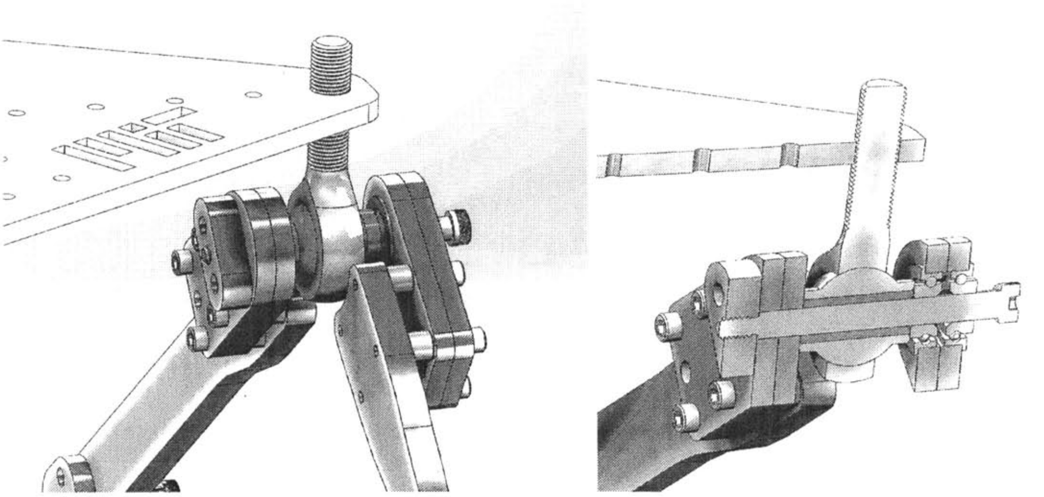

Figure 5-6: Regular and Section view of the Ball joint interfacing the top of each scissor mechanism with each apex of the top platform.

possible by the top platform. Super-Swivel ball joints were chosen, allowing the top platform to rotate with an angle range of ±32°.

The top joint of each scissor mechanism has a similar design to the other joints: A shoulder bolt passing through twin flanged roller bearings in a back-to-back configuration. The distance between each half of the scissor is extended using plates and standoffs, and the ball joint also passes through the shoulder bolt. A bronze spacer was used to interface the ball joint with the shoulder bolt.

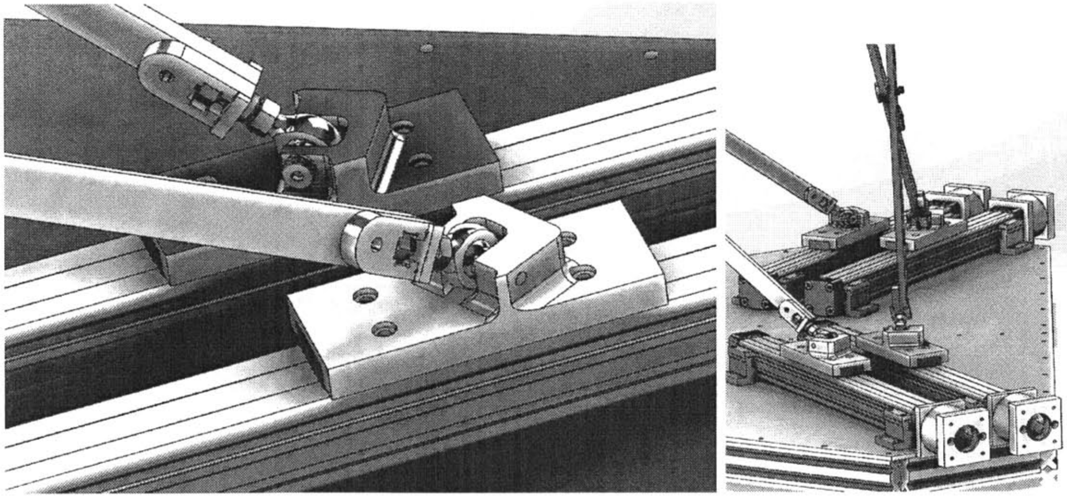

Figure 5-7: Plastic Bottom Ball Joint Adapters for coupling each scissor mechanism bottom ball joint to its respective linear actuator.

In order to interface the bottom ball joints of each scissor mechanism with the carriage of each linear actuator, a plastic Bottom Ball Joint Adapter was designed. (See Figure 5-7). A hole through which a shoulder bolt can pass allows the bottom ball joint to be pinned to the adapter. Four counterbore holes allow the adapter to mount to the top of its linear carriage. The hole where the shoulder bolt pin passes through each bottom ball joint was angled outward by $90° - \eta = 60°$ in order to maximize the range of motion of each scissor mechanism. The distance between the ball joint center and the center of stiffness of the linear carriage was minimized in order to minimize the moments the carriage must bear under load.

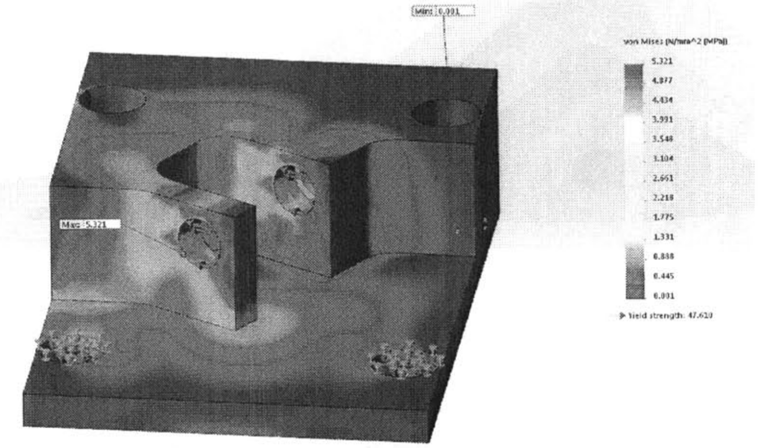

Figure 5-8: Finite Element Analysis of the Bottom Ball Joint Adapters.

The Bottom Ball Joint Adapter is designed to be 3D printed out of ABS plastic. In order to ensure that the plastic would not fail under load, a simulation of the internal stress in a Bottom Ball Joint Adapter under maximum loading was performed using Finite Element Analysis. As shown in Figure 5-8, the area with maximum stress is 5 times below the yield strength of the ABS plastic.

The Parker Origa ballscrew servo assemblies are mounted on a single plate in order to ensure the accuracy of the mounting holes relative to each other. The plate has additional support from 8020 extrusion ribs and lining. The final design is shown in Figure 5-9.

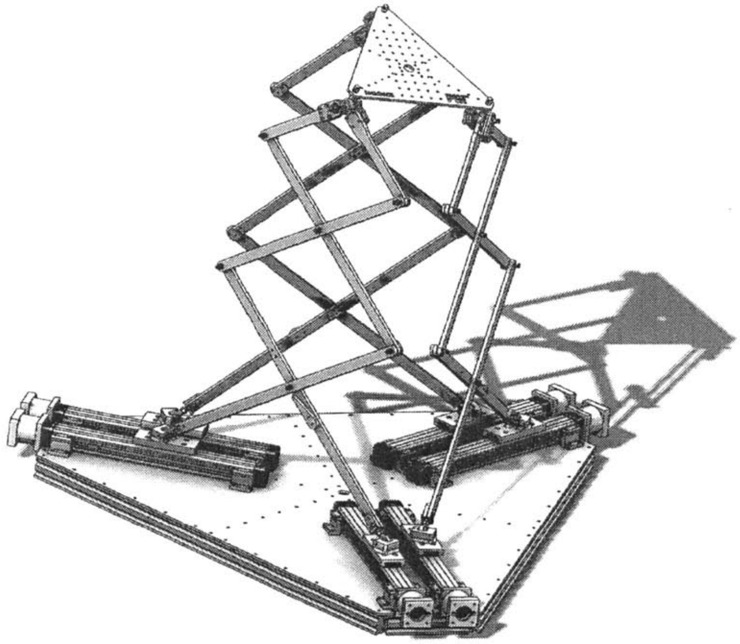

Figure 5-9: Solid Model Rendering of the Triple Scissor Extender

5.3 Manufacturing and Assembly

The TSE structural components were all designed to be easily cut on an Omax 5555 waterjet, with rapid manufacturing, minimal finishing operations, and quick assembly in mind.

The Omax 5555 waterjet (Figure 5-10) used to cut the structural components has a positioning accuracy of 0.001 inches with a 0.0010 inch repeatability, ensuring that each scissor mechanism is identical, and that all mounting holes for the ballscrew actuators are accurately positioned.

The links of the scissor mechanisms were cut from 0.375 inch thick 6061 Aluminum (See Figure 5-11). Material of this thickness will leave a significant taper in any holes cut on a waterjet, so these holes were purposely undersized in order to facilitate a finishing operation. Each hole for the bearings and shoulder bolts was finished using a reamer in order to achieve a transition fit.

The bottom platform was bolted onto an 8020 structure for increased stiffness. The 6 Parker OSPE linear actuators were bolted down to the bottom platform using

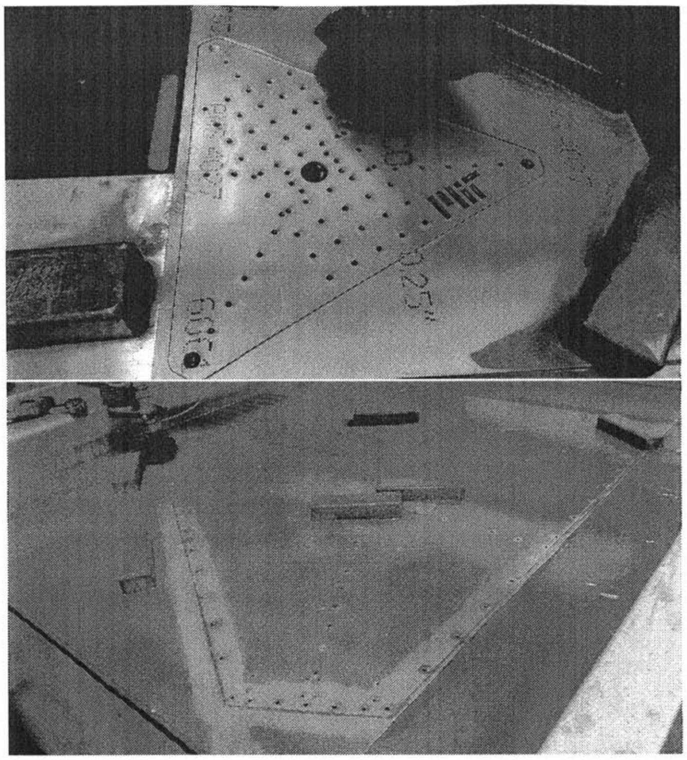

Figure 5-10: The Top and Bottom Plates being cut on an Omax 5555 waterjet.

the mounting holes cut on the waterjet to ensure alignment.

The 6 Bottom Ball Joint Adapters were 3D printed out of ABS Plastic on a Stratasys Dimension 1200es. They shoulder bolt shaft holes were finished using a reamer to achieve a transition fit, and the end was tapped to secure the shoulder bolt. Each adapter was then bolted onto the top face of the carriages of the Parker OSPE linear actuators.

The three scissor mechanisms were assembled (See 5-11), with each pin joint's bearings preloaded using a torque wrench to prevent damage to the flanged roller bearings. The tops of the three scissor mechanisms were pinned to the ball joints at the apices of the Top Platform. The Top Platform was then positioned in a raised configuration at the center of the base, and the bottom ball joints of each scissor mechanism were pinned to the Bottom Ball Joint Adapters of the linear actuators, to complete the assembly. The final assembly is shown in two configurations in Figure 5-12.

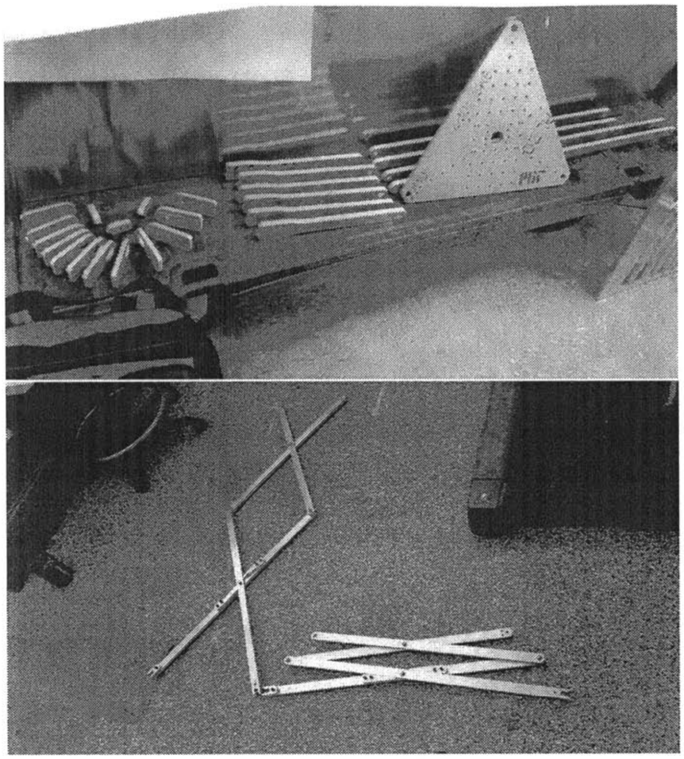

Figure 5-11: Set of scissor mechanism parts cut on the waterjet and partially assembled

5.4 Electronics, Controls, and Software

Each servo is driven and controlled by a Copley Accelnet panel (Figure 5-13). In order to facilitate untethered use, the system runs on four A123 12V7 ALM LiFePO4 battery modules in series, for a 52.8 Volt (48 Volt nominal) system. A 48 Volt LiFePO4 charger can be used to recharge the battery modules, and they have internal battery management systems for balancing and over/under voltage and current protection.

The six servo drives use a Kvaser Leaf CANopen USB Interface to communicate with a C++ control program running on a laptop running Ubuntu Linux 14.04LTS. This program leverages the C++ Motion Libraries (CML) provided by Copley for servo control and the Armadillo Linear Algebra Library [7] for computing the Inverse Jacobian $\mathbb{J}_I$ on-line.

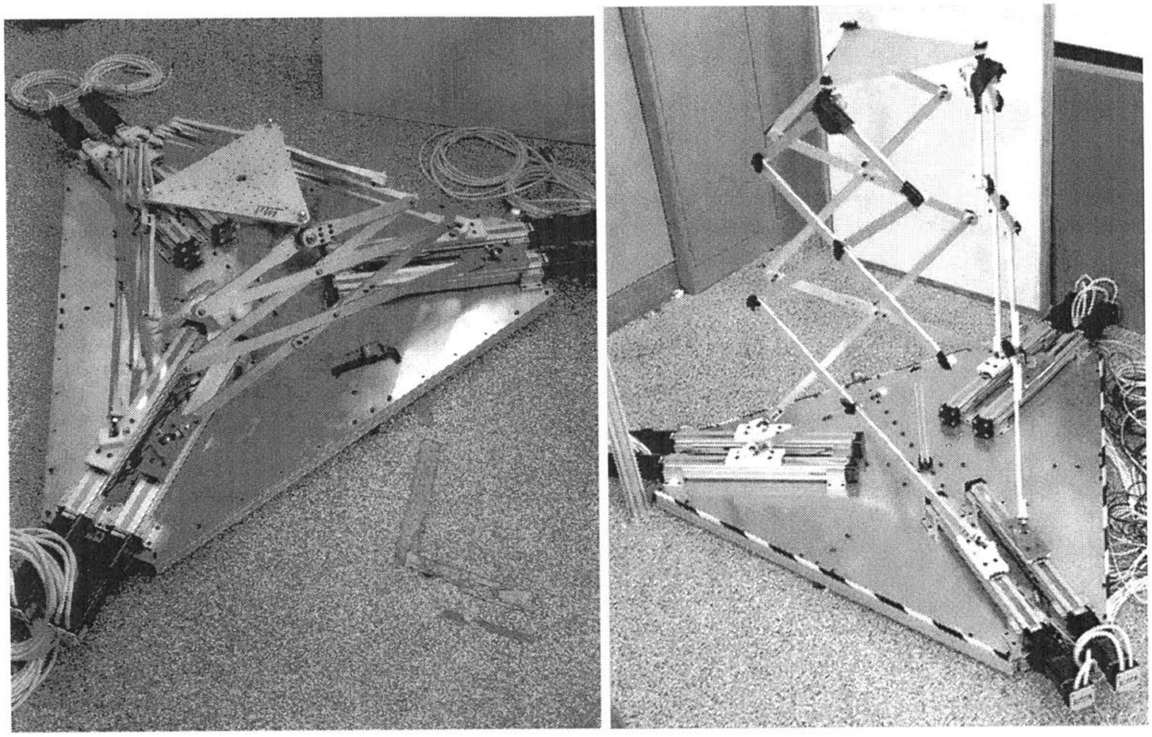

Figure 5-12: Experimental Prototype

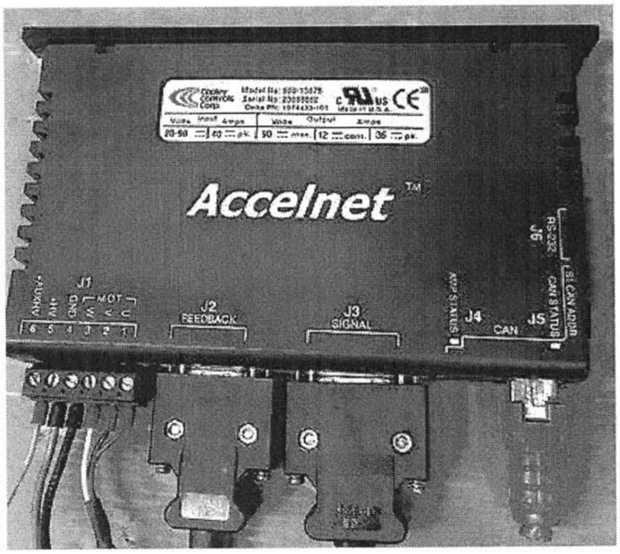
Accelnet™
J1
MOT
J2
FEEDBACK
J3
SIGNAL
J4
CAN
J5
CAN STATUS
J6
RS-232

Figure 5-13: Copley Controls Accelnet panel chosen to control and drive the Parker actuators.

Chapter 6

Experimental Validation of Differential Motion

6.1 Procedure

An experiment was conducted in order to evaluate the Inverse Jacobian's effectiveness for use in purely differential (stepping, or jogging) motion control of the TSE (See Figure 6-1). By beginning the experiment at a known state of actuator displacements q and top platform pose p, differential motion can be achieved by calculating the current Inverse Jacobian, multiplying it by a desired small change top platform pose, and commanding the actuators to move by that amount. For simplicity, only the horizontal configuration (no rotation) was considered.

The control program writes each new p and q to a file to create a dataset of desired states. The top platform's actual motion cam be measured using a motion capture system to create a dataset of actual states. An OptiTrack motion capture system consisting of four Flex3 cameras and a supporting structure was built around the TSE. OptiTrack Motive software was used to track markers that were placed at the three apexes of the TSE's top platform. These data were then exported and compared to the desired dataset to verify the Inverse Jacobian differential control scheme. A set of discrete translations in increments of 6.35 millimeters (0.25 inches) was performed about a central pose at a height of 1173.16 millimeters (46.1875 inches).

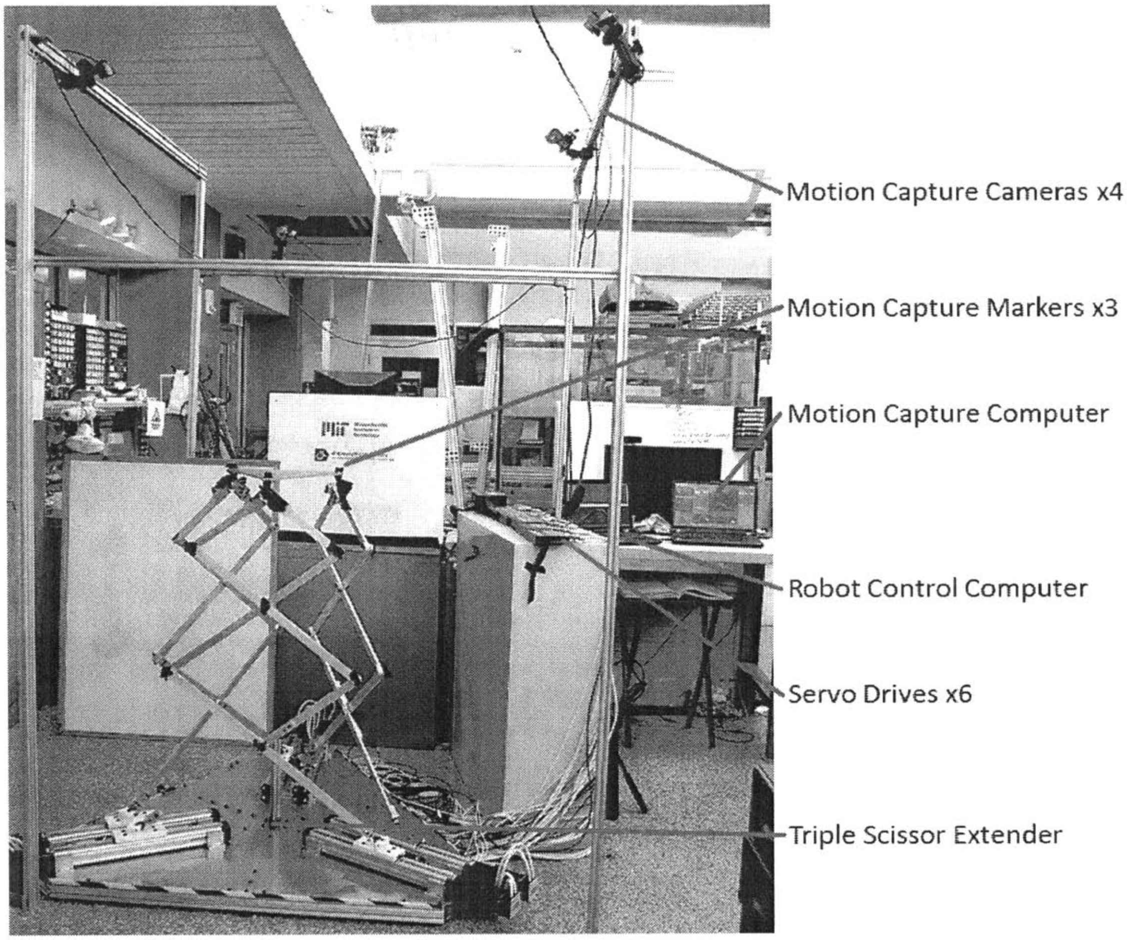
Motion Capture Cameras x4
Motion Capture Markers x3
Motion Capture Computer
Robot Control Computer
Servo Drives x6
Triple Scissor Extender

Figure 6-1: Experimental Setup

6.2 Results

Figure 6-2 shows that the top platform consistently moves the same amount in each axis, but does not move the desired amount. This reveals a systematic error, either in the model or in the control architecture. The model does not take into account the passive structural mechanics such as the mass and stiffness of the individual components of the TSE and how gravitational loading may alter the modeled versus the actual position.

Another possible source of error could be that the experimental jog amount of 6.35 millimeters is too large to allow for first-order control about the point. As the Jacobian is effectively a linearization about some operating point, this first-order

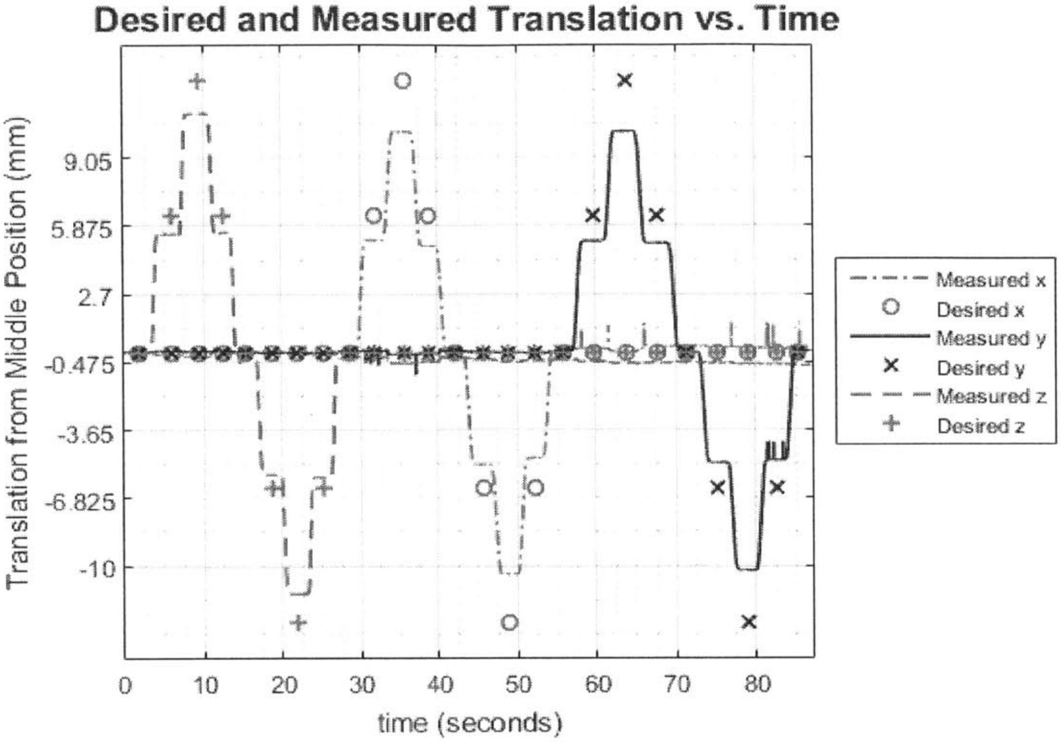

Figure 6-2: Top Platform Desired and Measured Translation vs Time

approximation may not properly capture the nonlinear kinematics of the TSE at the scale of the jog amount. To resolve this, the jog amount would need to be decreased so that a new Inverse Jacobian calculated more often between motions, smoothing out the kinematic nonlinearities.

Regardless of the cause of error, endpoint feedback using a motion capture system or some other external sensing could be used to obtain full closed-loop control of the TSE and eliminate any remaining error. The TSE using the Inverse Jacobian with either a passive structural mechanics model, fully continuous Jacobian calculation and motion integration, and/or closed-loop endpoint feedback control would be able to reach any pose within its workspace.

Chapter 7

Extending Functionality with Detachable End Effectors: FASBots

7.1 FASBot Requirements

The Triple Scissor Extender [1] was designed for autonomous fastener installation. With its large height range, it can reach any location along the inside of the fuselage structure, but its effectiveness can be extended through process parallelization. The Triple Scissor Extender (TSE) can act as a parent robot, picking and placing a number of child robots that couple to features along the inside of the aircraft. That way, a single TSE can transfer as many child robots as are needed by the outside robots performing the drilling, reaming, countersinking and insertion operations.

This concept has been explored by Boeing using a suction system [8], but improvements in machine coupling can be made to improve the child robot's positioning repeatability. In order to ensure that the child robot repeatably aligns with respect to the fasteners every time it attaches to the airframe, a coupling mechanism using design insight from kinematic couplings can be used.

A machine was developed using a deterministic design process [9] in order to achieve a predictably high-performing and robust solution to the problem of parallelizable local fastener installation.

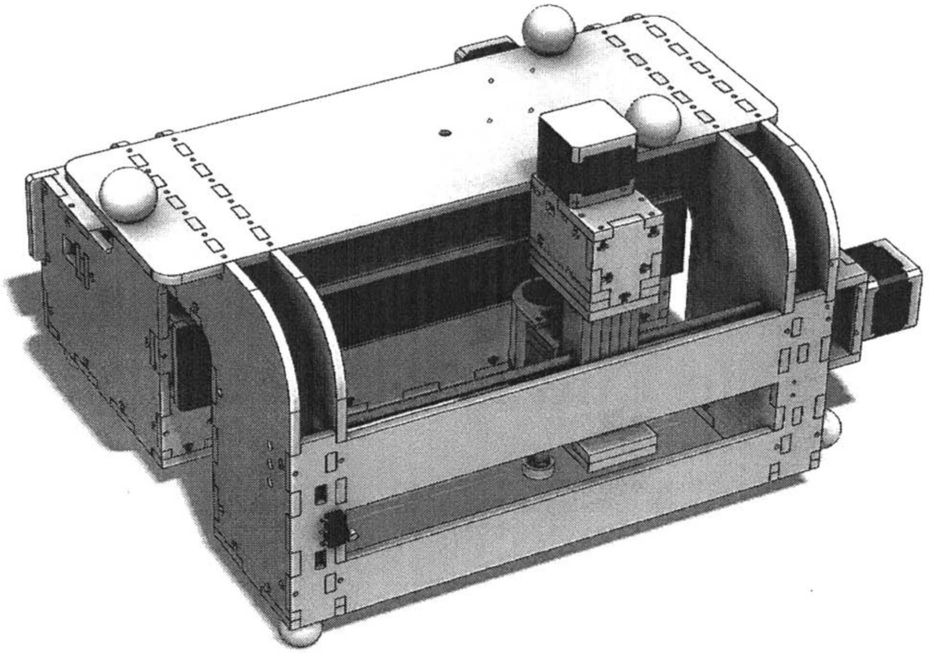

Figure 7-1: The final FASBot CAD rendering.

We call this machine a FASBot, or FAStening roBot (See Figure 7-1).

The FASBot Functional Requirements are as follows:

- The FASBot must attach itself to features on the inside of the airframe.
- It must align with respect to the fasteners without an external sensing process.
- It must access the area where the shear ties are fastened.
- It must hold and actuate the nut driver tool.
- It must not fall and break itself, the aircraft, or people.
- It must not otherwise damage the aircraft.
- It must be able to precisely position the nut driver tool along the shear tie and fasten at least six fasteners in a row.

- It must not deflect the shear tie during the outer robot drilling, reaming, countersink, and insertion operations.
- It must handle fastener insertion misalignment up to 0.010 inches.
- It must couple to and attach to the Triple Scissor Extender.

7.2 FASBot Detailed Design

7.2.1 Clamping and Axis Design Details

The most critical module of the FASbot is the clamping mechanism. Without a reliable clamp, the FASBot would fall and potentially break, may harm the aircraft being assembled, and may harm a worker.

In order to clamp against gravitational loading, a frictional model must be attained. If there are two clamps, each with two contacts against the shear tie, then there are four surfaces total engaged.

$$F_g = 4\mu_{static}F_{clamp} \tag{7.1}$$

The holding torque of the NEMA 17 stepper motor is 0.45 Newton-meters. The motor has a resolution of 1.8° per step, or 200 steps per revolution. If we desire a positioning accuracy of 0.0005 inches, then we need a transmission ratio that moves the carriage at most 0.1 inches per motor revolution. The minimum pitch of a leadscrew would be 10 threads per inch.

With this transmission method, the maximum force out would be 1110 Newtons. If we assume 25% transmission efficiency, then 277.5 Newtons can be applied to the carriage.

To decide on a minimum leadscrew size, buckling must be taken into account. The following formula may be used to determine the force required to buckle a beam with Young's Modulus E, cross-sectional second moment of area I, and length L. In the fixed-rounded boundary conditions, $n = 2$.

$$F_{buckling} = \frac{n\pi^2 EI}{L^2} \tag{7.2}$$

If $E = 200$ gigapascals, $F_{buckling} = 1110$ Newtons, $L = 12$ inches, and the second moment of area $I = (pi/4)r^4$ then $r = 0.09455$ inches.

A 1/4-16 ACME leadscrew was selected because it is a standard size with a smaller pitch and a greater diameter than is required. A pitch this small is not backdrivable, allowing the clamps to remain engaged in the case of a power failure. For parts interchangeability, both clamps and both axes will use the same leadscrew and linear rails.

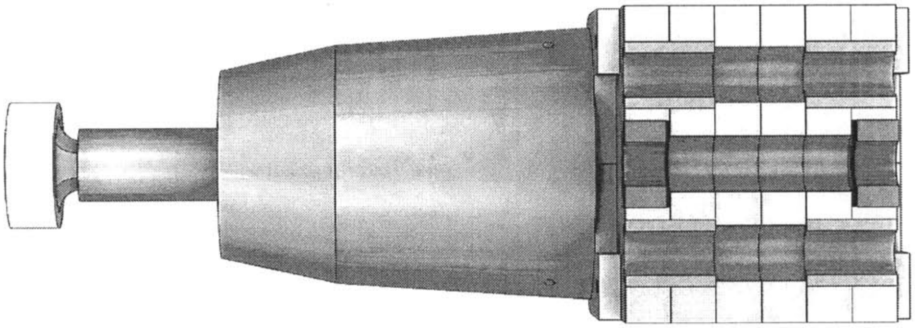

Figure 7-2: Section view of the Z-Axis. Both axes and clamps have the same linear carriage design.

For moving the carriage with the leadscrew, pair of ACME nuts are used, one at each end of the carriage. In order to prevent significant backlash, a wave spring is placed between each ACME nut and the carriage, pushing the nuts outward. This outward force allows the nut to always be engages with the outer face of the thread that pushes it. The axial stiffness of the carriage is equal to the stiffness of the ACME nut preload spring, making it a Type 2 anti-backlash system, as defined in [3].

The twin circular shafts pass through the carriage sleeve bearings and are constrained at the ends. The leadscrew is constrained axially from only one end to prevent overconstraint, and has radial support at both ends. A pulley allows a toothed belt

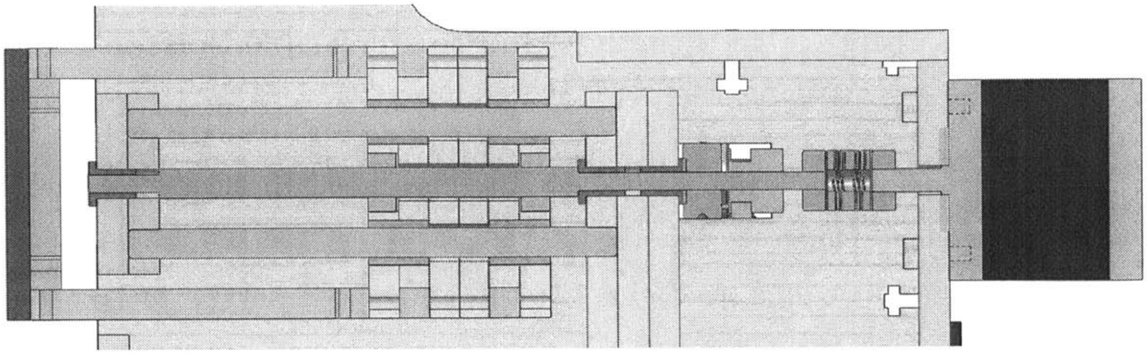

Figure 7-3: Section View of the driven Clamp Axis.

to transfer torque to a second identical clamp axis on the other side of the FASBot. A flexible shaft coupling couples the leadscrew to a stepper motor.

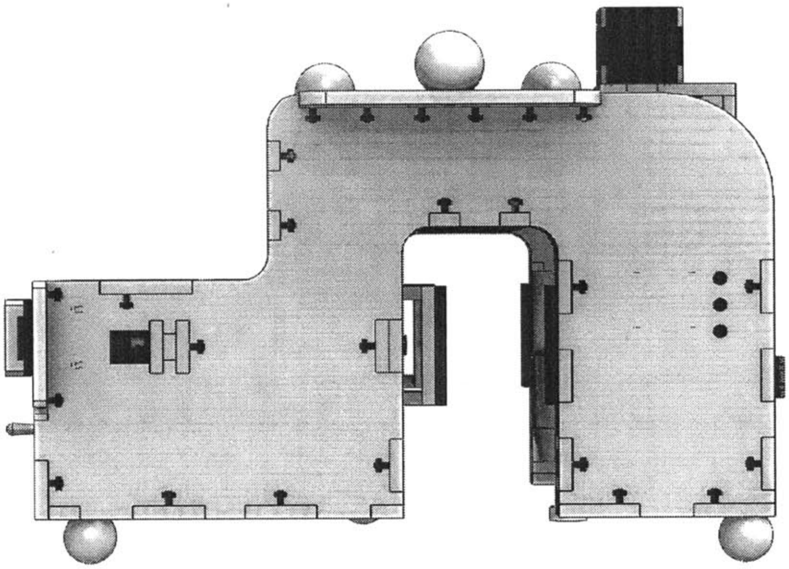

Figure 7-4: Side View Rendering of the FASBot.

The dimensions of the FASBot structure (Figure 7-4) were chosen based on an error analysis using the modeled machine stiffness.

7.2.2 Coupling to the Fuselage and to the Triple Scissor Extender

In order to reliably couple to the top of the TSE, a three-groove Kinematic Coupling is used. The grooves are located on the top platform of the TSE, and the FASBot has three balls at its top. A magnet on the TSE will provide sufficient preload to keep the FASBot attached to the TSE. The FASBot has a piece of steel at the center of stiffness to mate with the magnet.

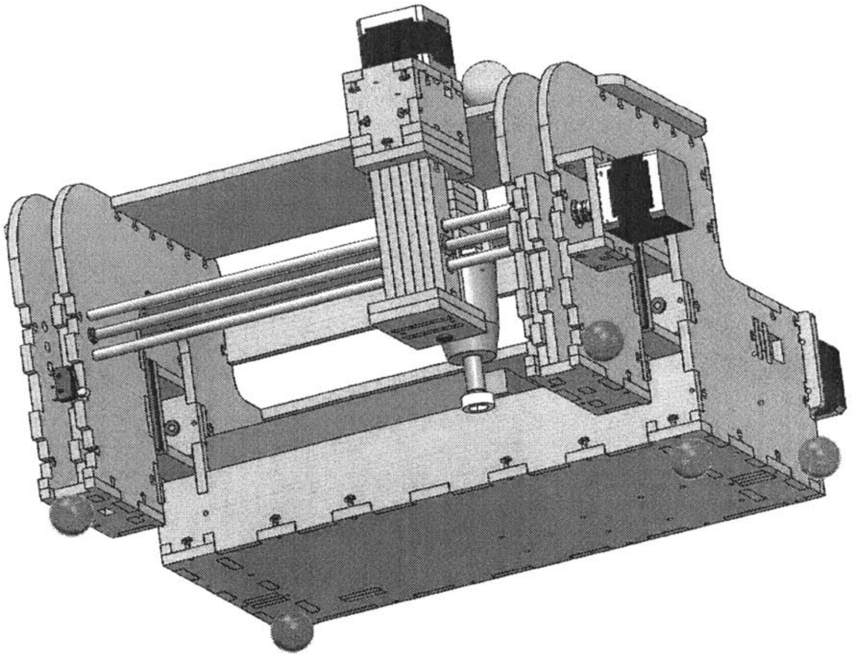

Figure 7-5: The five point contacts used for coupling to the fuselage.

In order to repeatably localize with respect to the aircraft's shear tie for the fastening operation, the FASBot utilizes 5 point-contact coupling features (See Figure 7-5) and an elastically averaged clamp [11] to couple all 6 DOFs top the fuselage (See Figure 7-6). The TSE will place the FASBot against the inner surface of the fuselage, and three balls will align the FASBot to the curved inner surface. When fully coupled, two of the three surface constraint balls are in a line so that the FASBot can couple to a fuselage section of any radius.

The TSE then pushes the FASBot up, until two additional balls align the FASBot

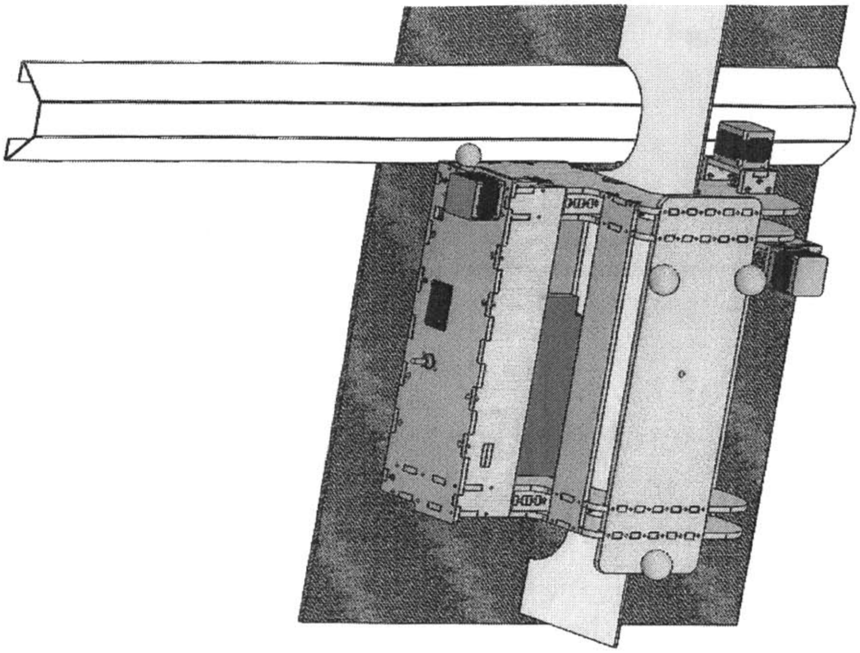

Figure 7-6: CAD Rendering of the FASBot clamped to the fuselage facade.

to the trapezoidal stringers to constrain the FASBot upward motion and rotation. Finally, the TSE pushed the FASBot left until the two inner clamp surfaces contact the stringers. Then, the clamps close while the TSE preloads the FASBot against the fuselage, securing the FASBot to the fuselage. The TSE can then pull away from the FASBot safely, and the clamp force overcomes the magnetic preload force.

The FASBot is then perfectly aligned with the first fastener location, and can begin to perform the fastening operation in conjunction with the outside robot. Because of its kinematic nature, this localization process is repeatable without the need for sensing and is robust to errors in the positioning of the TSE.

7.3 FASBot Manufacturing and Assembly

The FASBot was designed with rapid manufacturing and assembly in mind, minimizing the need for manually machined components.

All structural components were cut from 0.250 inch thick Medium Density Fiber-

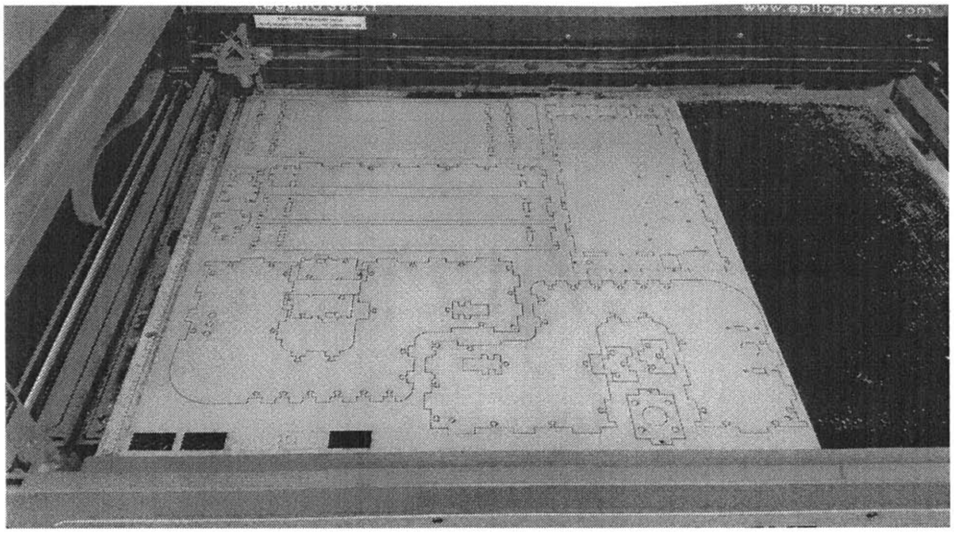

Figure 7-7: The components were cut from an Epilog lasercutter.

board (MDF) using an Epilog lasercutter (See Figure 7-7). For components requiring tight tolerances (such as the axis parts holding the ACME nuts and linear motion bushings), test parts were cut and measured to compensate for the kerf of the lasercutter. This ensured that all of these components would maintain transition fits with the nuts and bushings, and no preload from a press fit would cause unwanted frictional forces would cause the axes to bind.

Each axis, like that in Figure 7-8 was assembled by stacking the components, inserting the nuts and bushings, and passing the twin rails through them and fixturing them to the main structure before tightening the bolts. The ACME nuts are pressed in toward each other while the ACME leadscrew is threaded through the carriage in order to eliminate backlash. Torsional compliance of the X-axis was exploited to allow for passive motion in the Y-axis to account for any misalignment from the manufacturing process.

The two clamp axes were zeroed against the end of their travel, and the belt was installed (See Figure 7-9). Two bearings and an idler pulley allow the belt to be tensioned in order to ensure tracking between the leader and follower clamps.

The electronics compartment is shown in Figure 7-10. FASBot runs off of a 22.2 Volt Lithium Polymer battery. A linear regulator steps down the voltage to 12 Volts

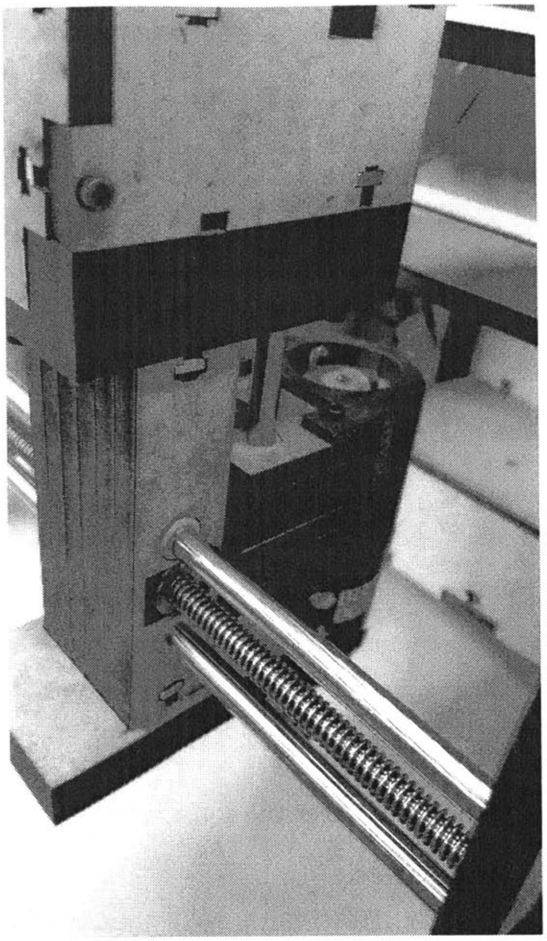

Figure 7-8: Closeup of the X and Z axes after assembly.

for the Arduino Uno microcontroller. The CNC Shield uses the 22.2 Volts to drive the stepper motors and the spindle. A pair of XBee wireless communication modules are used to facilitate wireless serial communication between a host computer and the FASBot. The Arduino Uno on the FASBot an XBee Shield, and the host laptop has an Xbee USB adapter. A Python program sends GCode commands to the FASBot.

The electronic components were all bolted to the FASBot structure using non-conducting fasteners. The battery was secured to the structure using adhesive hook-and-loop fasteners. All wiring was secured using adhesive ziptie holder blocks so that no components shake or rattle when the FASBot is carried.

The final assembled FASBot (See Figure 7-11) weighs about 5 pounds.

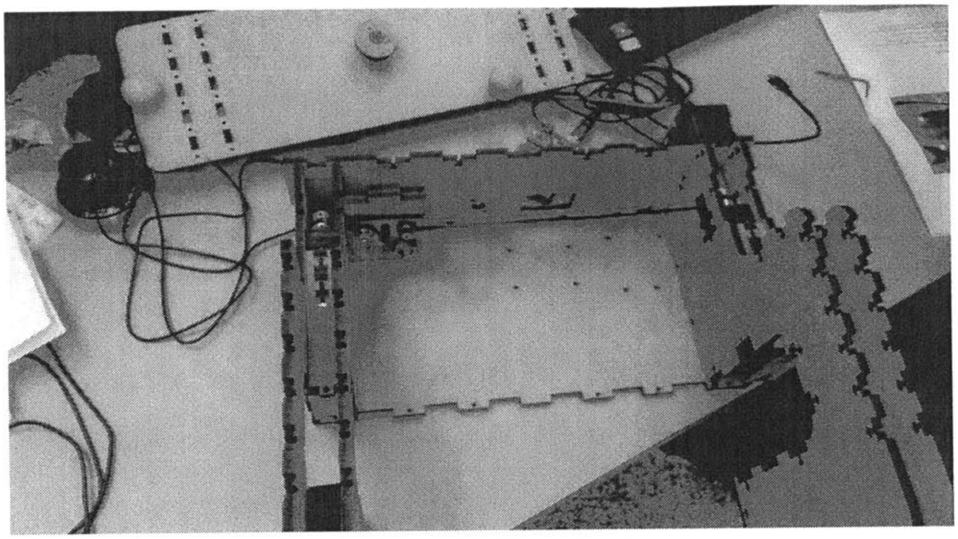

Figure 7-9: The twin clamp axes assembled with the timing belt that couples their motion.

7.4 FASBot Testing and Results

The fuselage facade 7-12 is modeled after the longitudinal stringers and the circumferential shear ties found on a Boeing 787, used to test and demonstrate the FASBot with the Triple Scissor Extender. The clamp axis provided sufficient force to hold the FASBot inverted against gravitational loading and other disturbance forces. The clamping force overcomes the magnetic preload from the FASBot-to-TSE kinematic coupling, allowing the TSE to safely disengage from the FASBot and perform other tasks.

The axis positioning repeatability and backlash were tested to validate the module's design. Because both the clamp and nut driver axes are based on the same design, and because most axes are hard to reach or instrument, These tests were conducted on the X-axis.

In the positioning accuracy test, the FASBot consistently moved slightly under the 0.005" it was commanded to move, implying a systematic error. This is possibly due to rounding errors in the conversion from millimeters to inches in the grbl firmware. This error can be eliminated using feedback control.

The backlash was tested by jogging the axis left after having moved it over 1 inch

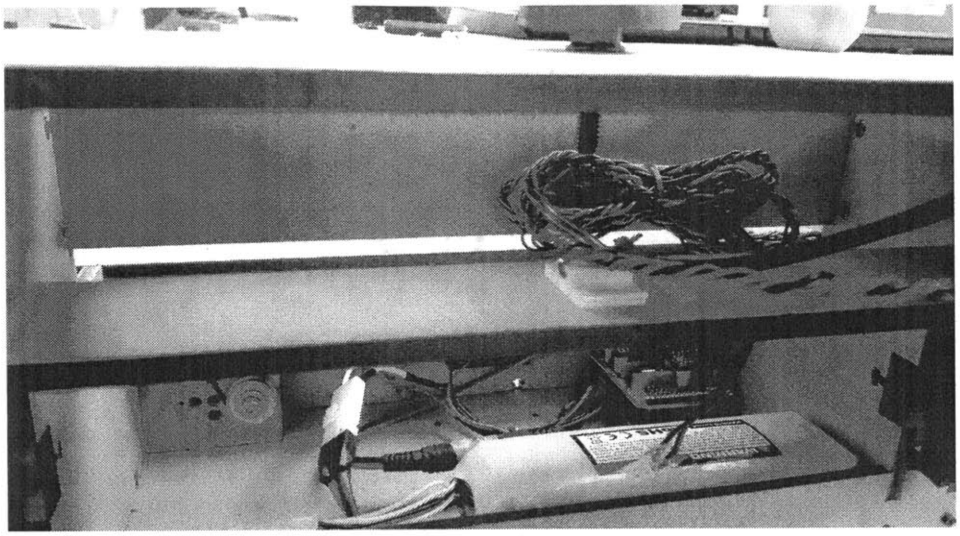

Figure 7-10: The electronics compartment of the FASBot.

to the right. By counting the number of jog commands before the axis began to move in the new direction, the backlash was determined to be 0.025 inches. This is probably due to the exact locations of the tooth engagement and the series spring compression. This problem can be eliminated by using a stiffer spring with a longer stroke, or by disassembling the axis and finding the right combination of nut pair rotations that allow for the most spring compression and the least backlash. While feedback control with a hysteresis model can account for the backlash, it won't perform as well as a zero-backlash system with feedback control.

The repeatability test involved the FASBot continually moving its X-axis between 4 inches and 3 inches in order to move past the backlash hysteresis. The dial indicator was zeroed for the first data point reaching 4 inches. Each data point was measured using the dial indicator and manually entered into a spreadsheet when the carriage came to a stop.

The results of the repeatability test are shown in Figure 7-15. 3 Test Trials were conducted, with the FASBot being homed after each one.

Tests 1 and 2 exhibit similar behavior, with the machine always moving farther and farther away from the original position. Test 2 was the worst, with a maximum deviation of 0.035 inches, more than the axis backlash. This behavior may be at-

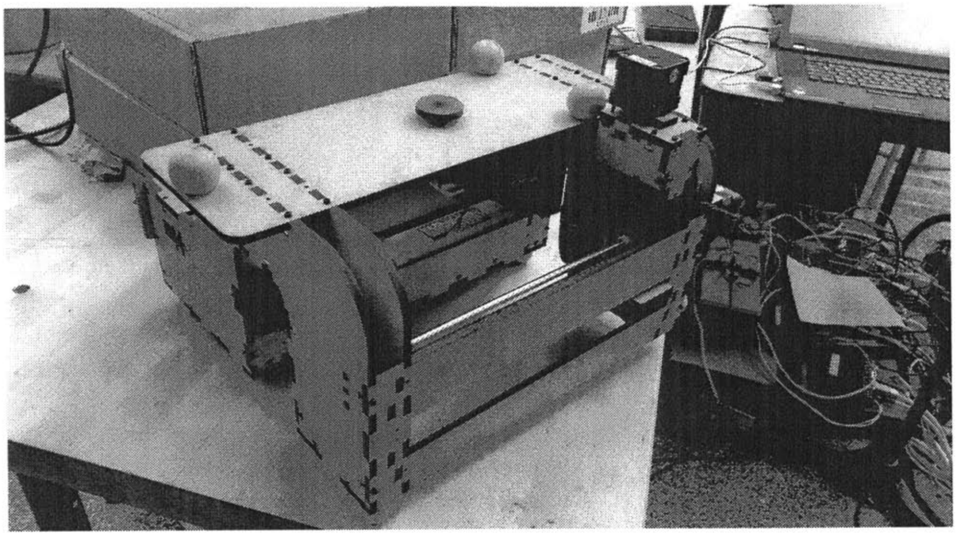

Figure 7-11: The fully assembled FASBot.

tributed to the stepper motor skipping steps every time it moves, perhaps because it must overcome static frictional torque. If the axes are overconstrained, one axis bushing can be relieved by mounting it on a flexure or by milling the inner sides that overconstrain its motion.

Microstepping may have also be useful to prevent skipping steps due to motor vibration. These tests were conducted with, in order to maximize motor torque, but the sharp vibrations in the stepper motor during acceleration/deceleration could have been enough to cause skipping. By switching to half- or quarter-stepping, smoother motion can be achieved with no continuous deviation. All of the repeatability error can be eliminated using feedback control.

The best repeatability was achieved in Test 3, with a maximum deviation of ±0.0055 inches.

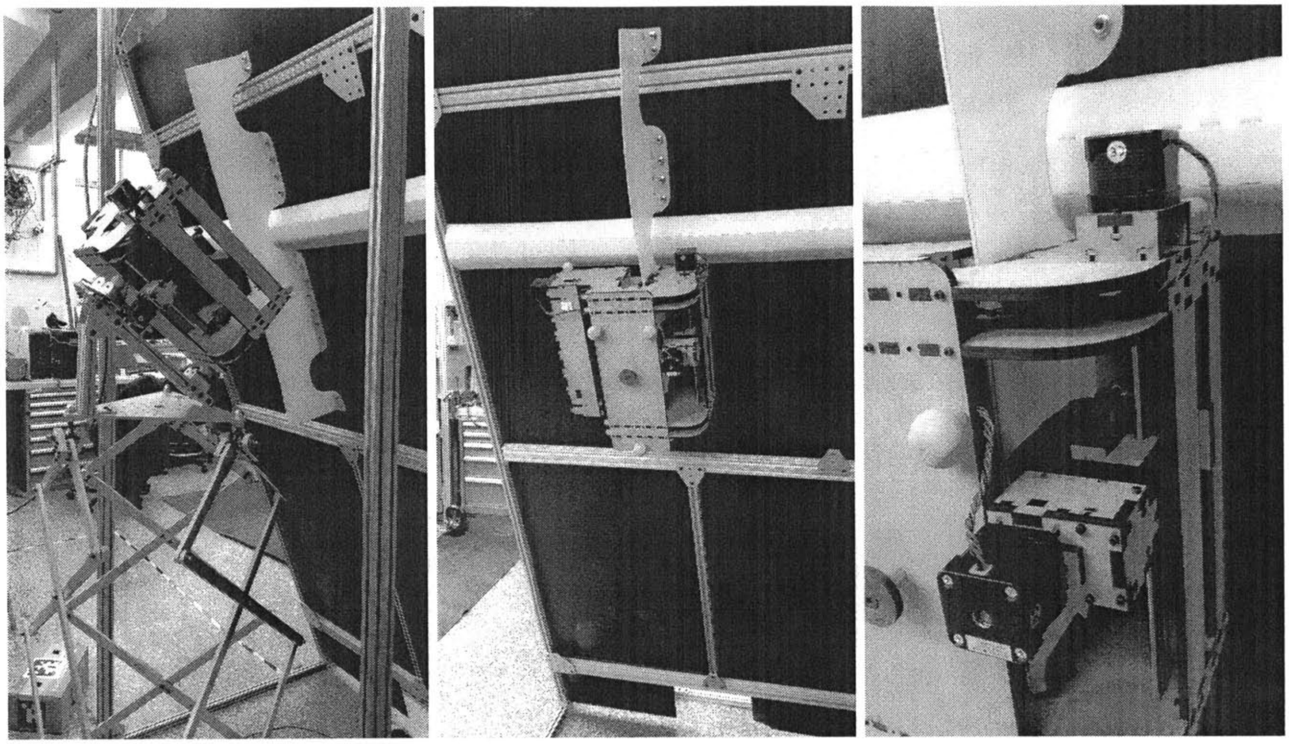

(a) FASBot on TSE (b) FASBot Coupled to Wall (c) FASBot Tool over Fastener

Figure 7-12: The FASBot during the various stages of use.

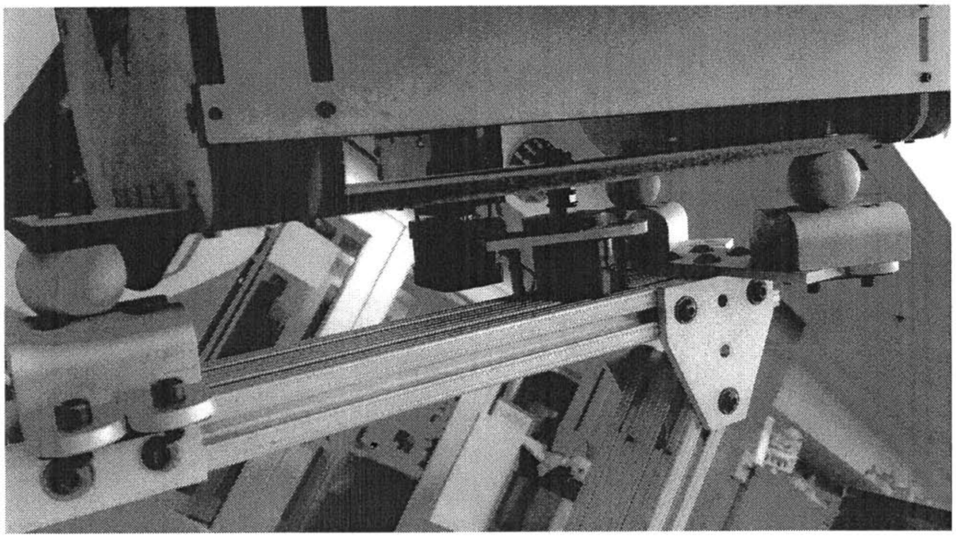

Figure 7-13: The Three-grooves/three-ball FASBot-to-Triple Scissor Extender Kinematic Coupling.

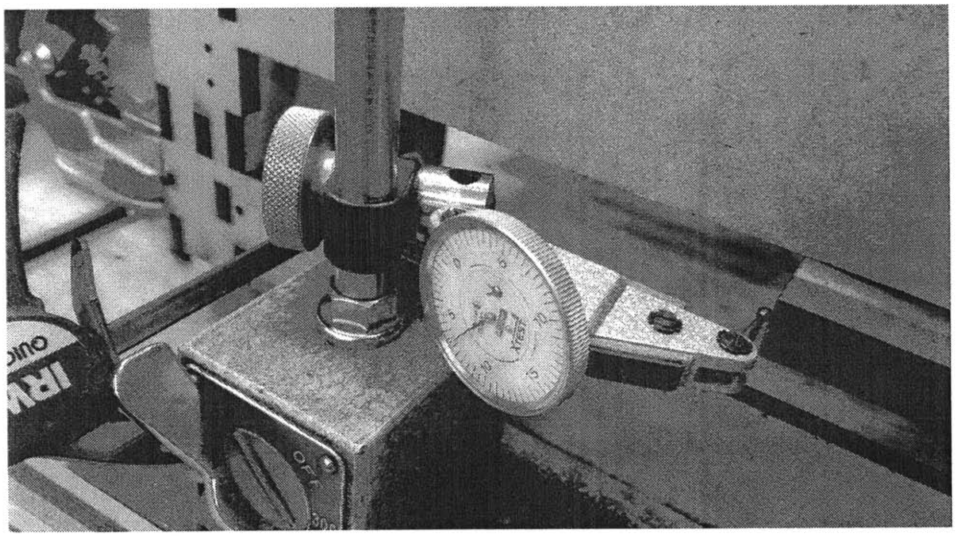

Figure 7-14: The experimental setup for testing axis repeatability.

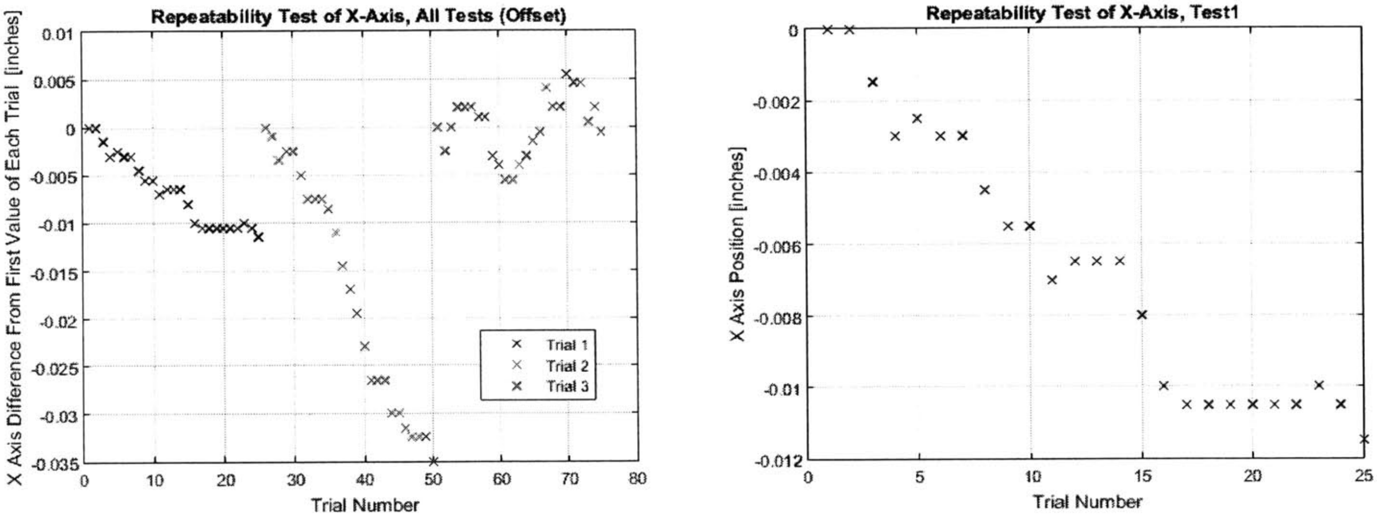

(a) All Tests

(b) Test1

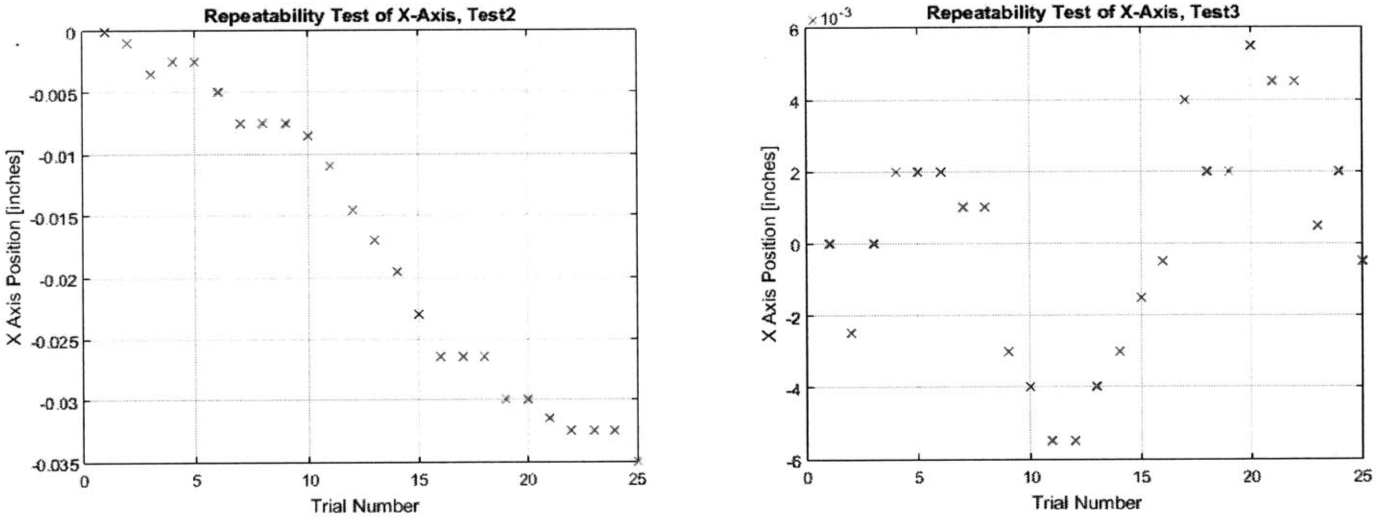

(c) Test2

(d) Test 3

Figure 7-15: Three runs of the repeatability test, combined and individual plots.

Chapter 8

Conclusion and Future Work

8.1 Conclusion

The Triple Scissor Extender (TSE) is a novel 6-DOF robot that can reach both high ceilings and low to the ground. It achieves height amplification through the use of scissor mechanisms, and can reach any pose in its workspace through the coordinated motion of linear actuators located at the base.

Using the Kinematic Constraint Equations, the Inverse Kinematics can be solved given the implemented design parameters, allowing the TSE to be commanded to move to any point in its workspace. The Spatial Gear Ratio defined by the eigenvalues of the Inverse Jacobian matrix provides useful information about the configuration-dependent motion and behavior of the TSE. The design parameters that govern the motion of the TSE can be modified to change the TSE's height amplification properties, and configuration-dependent translational and rotational motion behavior.

A prototype of the TSE was designed and built in order to amplify motion by 5 times and reach up to 63.75 inches. The prototype made use of commercial off-the-shelf components and a structure made of Aluminum that was cut on an Omax waterjet. A differential motion and inverse kinematic control program was written to command the prototype using a computer.

Tests were conducted on the TSE prototype to validate the differential motion control scheme. Systematic errors were found to be caused by unmodeled structural compliance.

The functionality of the TSE was expanded with Fastening Robots (FASBots) enabling a single TSE to manage multiple FASBots that perform manufacturing operations. A prototype FASBot was designed to couple to the TSE and clamp to the inside of a mockup Boeing 787 fuselage. The prototype was built and successfully performed the clamping and fastening task while working in conjunction with the TSE.

In addition to aircraft manufacturing, the TSE may be used for many other applications requiring 6-DOF end effector motion where a greater workspace than a traditional Stewart platform is required.

8.2 Recommendations for Future Work

As a machine tool, the Triple Scissor Extender would need to meet high stiffness requirements . Modeling and validating the stiffness of the TSE

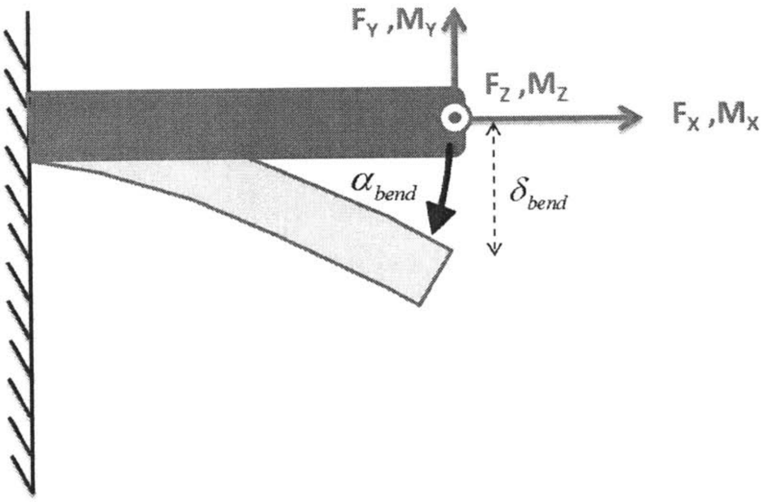

Figure 8-1: Example of Error Modeling for Stiffness Analysis of a single Beam

For example, a single beam's stiffness properties can be modeled for axial forces and moments, and bending forces and moments (See Figure 8-1). These forces can be propagated along the entirety of a structure made up of any number of rigid links as in Figure 8-2. The resultant deflections from these forces can than be propagated forward until the total endpoint angle and deflection are measured. A combined stiffness matrix between the endpoint and the base platform can then be solved for, allowing the TSE to be positioned to configurations where its stiffness or compliance may be optimal for a given task.

Dynamic analysis can be performed given the stiffness properties of the TSE. Controllers can be designed to compensate for the high-frequency system dynamics due to structural compliance in order to achieve high-speed tracking with the end-effector. Endpoint position and force feedback can also increase the performance and functionality of the TSE controllers.

An optimized redesign, given the design parameter sensitivity insight from Chapter 4 and the above stiffness analysis, would be another next step. The scissor mechanisms can use CNC milled linkages and stiffer bearings to increase performance. Custom linear slides can be designed and built to the exact specifications required for the task, and can be integrated into the base platform. The motor drivers and batteries can be integrated into the bottom platform and wheels can be added, making the TSE a mobile robot, able to maneuver around factory floors in order to perform tasks autonomously.

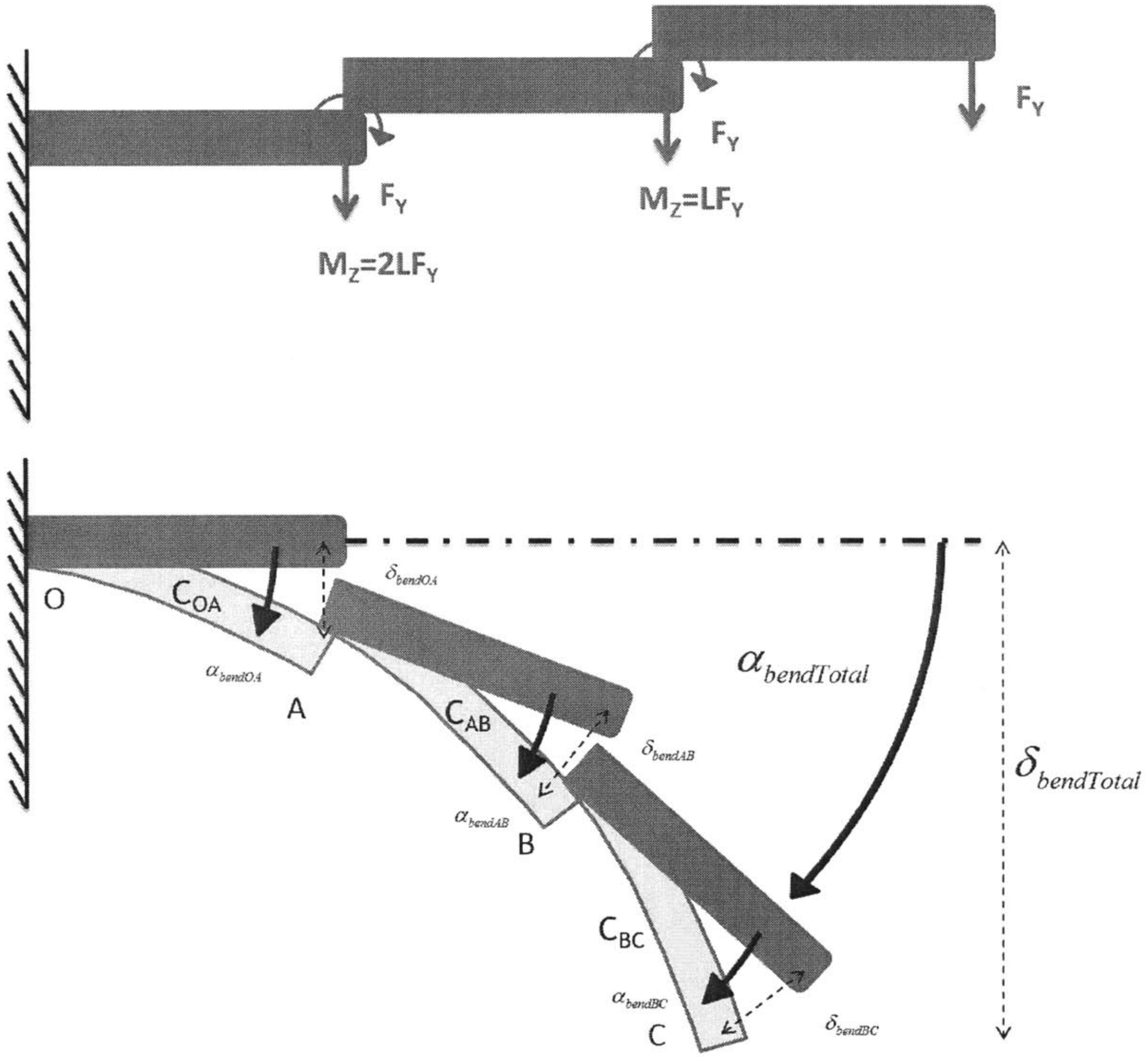
F_Y
F_Y
F_Y
$M_Z=LF_Y$
$M_Z=2LF_Y$
O
C_{OA}
δ_{bendOA}
α_{bendOA}
A
C_{AB}
δ_{bendAB}
α_{bendAB}
B
C_{BC}
α_{bendBC}
C
δ_{bendBC}
$\alpha_{bendTotal}$
$\delta_{bendTotal}$

Figure 8-2: Example of Error Modeling for Stiffness Analysis for a cascaded series of beams

Bibliography

[1] Daniel J Gonzalez and H Harry Asada. Triple Scissor Extender : A 6-DOF Lifting and Positioning Robot. In *Proceedings of the IEEE International Conference on Robotics and Automation*, 2016.

[2] Eric Gough. Contribution to discussion of papers on research in Automobile Stability, Control and Tyre performance. In *Proceedings of the Institution of Mechanical Engineers: Automobile Division*, pages 392–394, 1956.

[3] Layton C. Hale and Alexander H. Slocum. Design of anti-backlash transmissions for precision position control systems. *Precision Engineering*, 16(4):224–258, 1994.

[4] D. Jakobovic and L. Jelenkovik. The Forward and Inverse Kinematics Problems for Stewart Parallel Mechanisms. 2002.

[5] Anthony A. Maciejewski and Charles A. Klein. The Singular Value Decomposition: Computation and Applications to Robotics. *The International Journal of Robotics Research*, 8(6):63–79, 1989.

[6] J P. Merlet. Jacobian, Manipulability, Condition Number, and Accuracy of Parallel Robots. *Springer Tracts in Advanced Robotics: Robotics Research: Results of the 12th International Symposium ISRR*, 28:175–184, 2007.

[7] C. Sanderson. Armadillo: An Open Source C++ Linear Algebra Library for Fast Prototyping and Computationally Intensive Experiments, 2010.

[8] Branko Sarh. Method for coupling first and second structure, 2004.

[9] Alexander H. Slocum. *FUNdaMENTALS of Design*. Cambridge, MA, 2007.

[10] D. Stewart. A Platform with Six Degrees of Freedom. *Proceedings of the Institution of Mechanical Engineers*, 180(Pt 1, No 15), 1965.

[11] Patrick J. Willoughby. *Elastically Averaged Precision Alignment*. PhD thesis, Massachusetts Institute of Technology, Cambridge, MA, 2005.

[12] Jian Yang, Xing Wang, and Xue Feng Chen. Dynamic Identification of a 3-PRS Parallel Robot with Scissor-Type Prismatic Joint: A Cloud-Based Approach. In *Mechanisms and Machine Science: Advances in Reconfigurable Mechanisms and Robots II*, pages 339–350. Springer, 2015.